



Northern California Chapter of the American Association of Physicists in Medicine
The Young Investigator's Symposium

Friday, May 27th, 2022

Via Zoom (Meeting ID: 97516402514, Password: 833574)

<https://stanford.zoom.us/j/97516402514?pwd=Q3hUU2xYRVNkay9velNaTHpUNW05Zz09>

11:45 – 12:00 P.M. Sign-In & Registration

12:00 – 01:00 P.M. Keynote Speech

Dr. Olivier Morin, Associate Professor, Department of Radiation Oncology at UCSF

01:00 – 4:00 P.M. Talks from young Investigators:

Students:

Yile Fang (UC Merced)

Fast and High Spatial Resolution X-ray Luminescence Computed Tomography Imaging

Yibing Zhang (UC Merced)

Oxygenation imaging in deep tissue with X-Ray luminescence computed tomography (XLCT)

Donghoon Kim (UC Davis)

Deep learning based parametric estimation of CBF and ATT from multi-PLD ASL

Kaitlyn Liang (Stanford)

Calibration and validation of a real-time oximeter for FLASH-RT experiments

Quincy Huynh (UC Berkeley)

Enabling High Sensitivity and Resolution with Optimized Broadband Receive Front End Design for Magnetic Particle Imaging, Spectroscopy, and Relaxometry

Renesmee Kuo (UC Berkeley)

In Vivo therapeutic cell tracking using Magnetic Particle Imaging to optimize solid tumor immunotherapies

Residents:

Ramish Ashraf (Stanford)

Film-Less Quality Assurance (QA) of a Robotic-Arm Linac Using a Scintillation-Based Imaging System

Young Investigator Program Director: Stan Benedict: shbenedict@ucdavis.edu

Young Investigator Program Co-Director: Amy Yu: amysyu@stanford.edu

Northern Calif Chapter AAPM: President: Jason Matney, Treasurer: Olga Stafford, Secretary: Lawrie Skinner, Board Member: Sarah McKenney

Kamal Singhrao (UC Francisco)

Development of Quality Assurance Metrics for Synthetic CT (sCT) Image Generation of Treatments Utilizing MRI-Only Simulation for External Beam Radiotherapy

Jose Ramos-Mendez (UC Francisco)

Towards the employment of nanodosimetric quantities in treatment planning for charged particle radiotherapy

Meghan Keohane (UC Davis)

Comparing spatial accuracy of catheter localization between stepping-transverse mode and twister-sagittal mode in transrectal ultrasound (TRUS) based high-dose-rate (HDR) brachytherapy for prostate cancer

Postdocs:

Naoki Dominguez Kondo (UC Francisco)

Monte Carlo Track-Structure study of DNA damage in supercoiled plasmids.

Yansong Zhu (UC Davis)

Simultaneous estimation of blood input function using a kernel method and its evaluation with total-body PET

Reimund Bayerlein (UC Davis)

Qualitative and Quantitative Validation of a Scatter Correction Method for Total-Body Positron Emission Tomography

Shengtian Sang (Stanford)

A Cross-Attention Method Based on Tumor-Feature-Templates for Segmenting Small Liver Tumors in CT Scans

SLAM competitions:

Neeladrisingha (Neel) Das (Stanford)

Cell GPS: Tracking cancer metastasis in real-time

Tushar Shinde (Stanford)

Neighbors, Trip and Packing

Shengtian Sang (Stanford)

Using deep connections to make model see more clearly

Jose Ramos-Mendez (UC Francisco)

Chasing FLASH (the mechanism)

Meghan Keohane (UC Davis)

Which ultrasound imaging mode can localize the needle better

04:30 – 5:00 P.M.

Award Ceremony

Young Investigator Program Director: Stan Benedict: shbenedict@ucdavis.edu

Young Investigator Program Co-Director: Amy Yu: amysyu@stanford.edu

Northern Calif Chapter AAPM: President: Jason Matney, Treasurer: Olga Stafford, Secretary: Lawrie Skinner, Board Member: Sarah McKenney

Yile Fang (UC Merced)

- **Fast and High Spatial Resolution X-ray Luminescence Computed Tomography Imaging**

Yibing Zhang (UC Merced)

- **Oxygenation imaging in deep tissue with X-Ray luminescence computed tomography (XLCT)**

Donghoon Kim (UC Davis)

- **Deep learning based parametric estimation of CBF and ATT from multi-PLD ASL**

Kaitlyn Liang (Stanford)

- **Calibration and validation of a real-time oximeter for FLASH-RT experiments**

Quincy Huynh (UC Berkeley)

- **Enabling High Sensitivity and Resolution with Optimized Broadband Receive Front End Design for Magnetic Particle Imaging, Spectroscopy, and Relaxometry**

Renesmee Kuo (UC Berkeley)

- **In Vivo therapeutic cell tracking using Magnetic Particle Imaging to optimize solid tumor immunotherapies**



“At first I was happy I made smart transgenic mice..”

Fast and High Spatial Resolution X-ray Luminescence Computed Tomography Imaging

Yile Fang¹, Yibing Zhang¹, Jeffrey N. Anker^{2,3}, Ge Wang⁴, and Changqing Li^{1*}

¹Department of Bioengineering, University of California, Merced, Merced, CA 95343, USA.

²Department of Chemistry, Clemson University, Clemson, SC 29634, USA.

³Department of Bioengineering, Center for Optical Materials Science and Engineering Technology (COMSET), and Institute of Environment Toxicology (CU-ENTOX), Clemson University, Clemson, SC 29634, USA.

⁴Department of Biomedical Engineering, Biomedical Imaging Center, Center for Biotechnology and Interdisciplinary Studies, Rensselaer Polytechnic Institute, Troy, NY 12180, USA.

*Corresponding Author: Changqing Li, Tel.: (209) 228-4777; Email: cli32@ucmerced.edu

Abstract

X-ray luminescence computed tomography (XLCT) is a hybrid molecular imaging modality combining the merits of both x-ray imaging (high spatial resolution) and optical imaging (high sensitivity to tracer nanophosphors). Using the precise location of the x-ray beam as a priori information in the reconstruction algorithm, narrow x-ray beam based XLCT imaging can achieve a high spatial resolution at the cost of a long acquisition time.

In this talk, we will discuss our work on improving the spatial resolution and the measurement speed of the narrow x-ray beam based XLCT imaging. To break the spatial resolution limit of previous study, we have introduced a scanning strategy with a scanning step size smaller than the x-ray beam size. Our numerical simulations and phantom experiments have demonstrated that the spatial resolution can be improved to close to the x-ray beam size. However, the promised high spatial resolution requires a large number of linear scan steps and leads to very long acquisition time, which limits its applications for *in vivo* imaging. To improve the imaging speed, we have proposed a continuous scanning scheme (stage moves continually and read position constantly) to replace the selective excitation scheme (stage stops at each predefined position). In addition, we have used a gated photon counter to replace the high-speed oscilloscope as the data acquisition device. Compared with the oscilloscope, the photon counter records much less data without losing any relevant information, which makes the data acquisition time much shorter. Our phantom experimental results have verified the feasibility of our proposed approaches and the capability of 3D XLCT imaging within a reasonable time, yielding a 16 times faster scanning speed compared with traditional XLCT system.

Lastly, based on all the work we have done in XLCT imaging, we are building a focused X-ray luminescence tomography (FXLT) imaging scanner with multi-wavelength measurement capacity. We are performing numerical simulations, phantom experiments, and *in vivo* experiments to evaluate its performance. Some results will be reported in this talk.

Oxygenation imaging in deep tissue with X-Ray luminescence computed tomography (XLCT)

Yibing Zhang¹, Yile Fang¹, Jeffrey N. Anker^{2,3}, Ge Wang⁴, Changqing Li¹

¹Department of Bioengineering, University of California, Merced, Merced, CA 95343, USA.

²Department of Chemistry, Clemson University, Clemson, SC 29634, USA.

³Department of Bioengineering, Center for Optical Materials Science and Engineering Technology (COMSET), and Institute of Environment Toxicology (CU-ENTOX), Clemson University, Clemson, SC 29634, USA.

⁴Department of Biomedical Engineering, Biomedical Imaging Center, Center for Biotechnology and Interdisciplinary Studies, Rensselaer Polytechnic Institute, Troy, NY 12180, USA.

*Corresponding Author: Changqing Li, Tel.: (209) 228-4777; Email: cli32@ucmerced.edu

Abstract

Oxygenation concentration of tissues is an important factor in culturing stem cells and in studying the therapy response of cancer cells. Bone marrow is a typical example of heterogenous hypoxia site where the adult stem cells are maintained. The hypoxic bone marrow is also the site to harbor cancer cells. However, the oxygenation concentration is very heterogenous in tissues like bone marrow and tumors. Thus, direct high-resolution measurements of molecular oxygen (O_2) would provide powerful means of providing insight into the conditions needed to successfully culture stem cells outside of the body and for monitoring the effectiveness of therapeutics. Currently available technologies, including PET, BOLD/TOLD MRI, and SPECT, have limited spatial resolution. Although two-photon phosphorescence lifetime microscopy (2PLM) can provide better resolution at the micrometer scale, the poor penetration of the visible light limits the possibilities of many pre-clinical/clinical applications.

In this work, we proposed an imaging approach to measure the oxygenation concentration in deep tissues, based on the XLCT system, with the combined strengths of the high chemical sensitivity of the probe and the high spatial resolution of the XLCT imaging. The oxygen concentration is sensed by x-ray excitable scintillators that have the oxygen-dependent spectrum of emitted optical photons. By taking measurements at two different wavelengths, XLCT can image the oxygenation concentrations in deep tissues at a spatial resolution of about the superfine x-ray beam size (up to 20 μm). We have performed the spectrum measurement with various phosphor films at different oxygen concentrations. All the films were measured with two different bandpass filters under different oxygen concentrations. From the experiment results, we have observed substantial measurement ratio changes at the two wavelengths when the oxygenation changed from 14% to 0%. In addition, we have developed a novel method to reconstruct the complex XLCT targets to increase the quality of the reconstructed XLCT images. This novel method has been validated with numerical simulations and will be evaluated in phantom experiments.

Title: Deep learning based parametric estimation of CBF and ATT from multi-PLD ASL

Authors: Donghoon Kim¹⁻², Megan E. Lipford³, Hongjian He⁴, Vladimir Ivanovic⁵, Samuel Lockhart⁶, Suzanne Craft⁶, Christopher Whitlow³, and Youngkyoo Jung¹⁻³

1. Department of Biomedical Engineering, University of California, Davis
2. Department of Radiology, University of California, Davis
3. Department of Radiology, Wake Forest School of Medicine
4. Center for Brain Imaging Science and Technology, College of Biomedical Engineering and Instrumental Science, Zhejiang University
5. Department of Radiology, Medical College of Wisconsin
6. Department of Internal Medicine, Wake Forest School of Medicine

Purpose: A hierarchically structured CNN algorithm has been developed to reduce the total scan time of multiple post labeling delays (multi-PLD) arterial spin labeling (ASL) by estimating both cerebral blood flow (CBF) and arterial transit time (ATT) maps from reduced timing information using a 3-dimensional convolutional neural network (CNN).

Introduction: Multi-PLD ASL has been used to estimate CBF and ATT maps more accurately with multiple PLDs. However, acquiring ASL images at multiple PLDs requires relatively long scan time compared to a single PLD. We propose a hierarchically structured 3-dimensional CNN (H-CNN) to estimate the CBF and ATT maps from the reduced number of PLDs as well as averages to reduce the total scan time of multi-PLD ASL scheme.

Methods: Twelve participants (age: 68.92 ± 6.87 years) had MRI including a multi-PLD pseudo continuous ASL (PCASL) sequence. Total 6 inversion times (TIs) were collected from 1800ms, with increments of 600ms and 6 averages per TI. TI is the summation of labeling duration and PLD. The labeling duration of PCASL was 1800ms except the shortest TI that had 1700ms. Corresponding PLDs were [100ms, 600ms, 1200ms, 1800ms, 2400ms, and 3000ms]. Each TI had a minimum TR: [2900ms, 3500ms, 4100ms, 4700ms, 5300ms, and 5900ms]¹. A single-shot 2D EPI acquisition was used to cover the whole brain (56x70x36 matrix size, 3x3x4mm resolution, and 27.5ms delay between slices). To create the ground truth reference images for CBF and ATT, a voxel-wise non-linear model fitting was applied using the ASL kinetic model². Randomly chosen 9 subjects were used for the network training and the remaining 3 were used for testing. CBF and ATT maps were estimated hierarchically because CBF is dependent on ATT, while ATT is an independent measurement in the ASL kinetic model². Figure 1 shows the structure of our H-CNN model. To test if the reduced number of PLDs can be recovered in the H-CNN, the perfusion weighted images (PWIs) with the reduced number of PLDs were used for the network training. To avoid any bias for choosing PLDs, all combinations of PLDs were tested. Additional tests were performed if the reduced number of averages can be recovered in the H-CNN. First N averages were sequentially chosen for the average reduction test. A conventional nonlinear model fitting method was compared with the H-CNN using the root mean square error (RMSE) as a primary evaluation metric. Total scan time reduction by the reduced number of PLDs or averages was calculated as the percent difference between theoretical total scan time compared to the full dataset.

Results: Based on the overall RMSEs of the nonlinear model fitting and H-CNN with the reduced numbers of PLDs or averages, our H-CNN outperforms the model fitting method when the numbers of PLDs or averages were reduced (Figure 2). Figure 3 shows the estimated CBF and ATT maps of one of the test subjects using the nonlinear model fitting and the H-CNN with the different numbers of PLDs or averages. The total scan time reductions by the reduced number of PLDs or averages were addressed in Table 1.

Discussion: CBF and ATT maps were successfully estimated from multi-PLD PCASL with the reduced number of PLDs or averages using the H-CNN. The proposed model showed a higher estimation accuracy than the conventional nonlinear model fitting method with the reduced numbers of PLDs or averages. In conclusion, a smaller number of PLDs or averages can be used in the processing to generate both CBF and ATT maps without significant discrepancy from the reference, which allows a significant total scan time reduction of multi-PLD PCASL scheme.

References:

1. Johnston, Megan E., et al. Multi-TI arterial spin labeling MRI with variable TR and bolus duration for cerebral blood flow and arterial transit time mapping. *IEEE transactions on medical imaging* 2015;34(6): 1392-1402.
2. Buxton, Richard B., et al. A general kinetic model for quantitative perfusion imaging with arterial spin labeling. *Magnetic resonance in medicine* 1998;40(3):383-396.

Acknowledgements: Wake Forest Alzheimer's Disease Research Center (NIH P30 AG049638) and an NIH Research grant (RF1 NS110043)

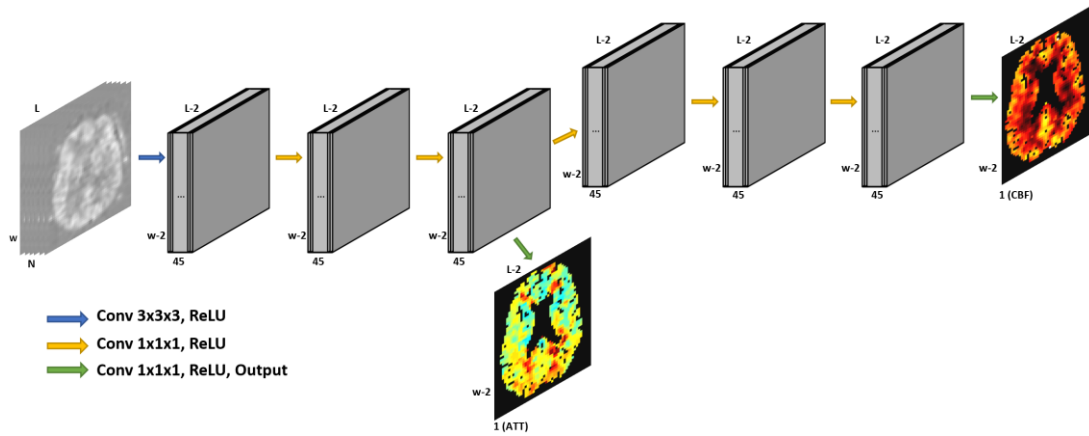


Figure 1. The structure of H-CNN. PWIs were used for the inputs where $L \times W \times H$ is the size of the PWI (the H dimension is not shown), and N denotes the number of PLDs. ATT was estimated from the shared three layers and CBF was estimated from the additional hidden layers.

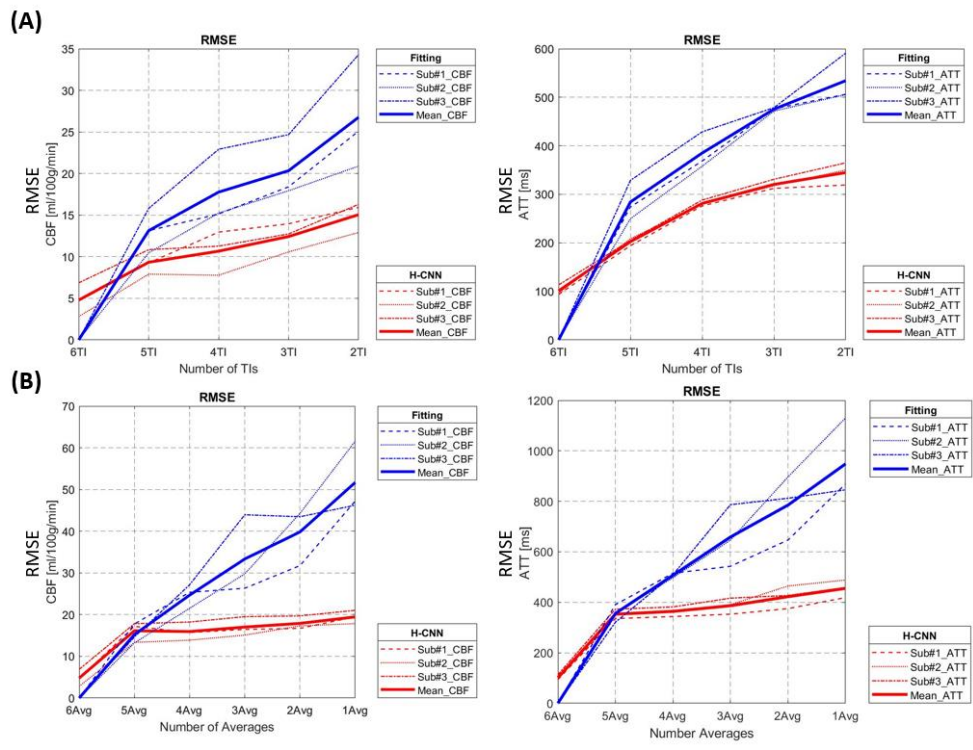


Figure 2. The overall RMSEs of the estimated CBF (left) and ATT (right) maps from the nonlinear fitting (blue) and H-CNN (red) using (A) the reduced numbers of PLDs and (B) the reduced numbers of averages. CBF and ATT maps from the nonlinear fitting with 6 PLDs and 6 averages were used for the ground truth reference images for the RMSE calculations. The reduced numbers of PLDs were selected based on the lowest mean of normalized RMSEs of the estimated CBF and ATT from the nonlinear model fitting and H-CNN separately.

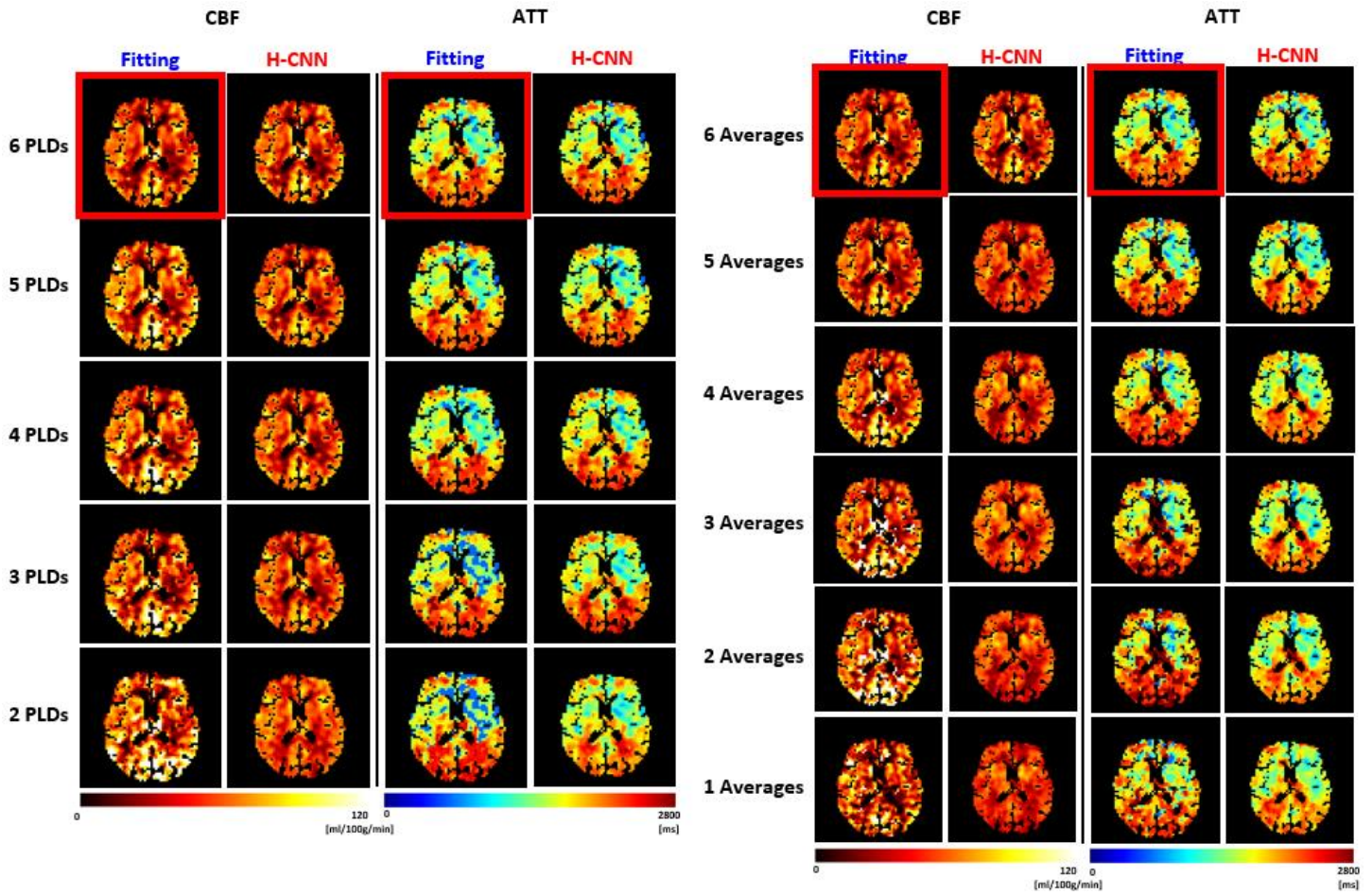


Figure 3. Estimated CBF and ATT maps from the nonlinear model fitting and H-CNN using the reduced number of PLDs (left) and averages (right). CBF and ATT maps (red boxes) from the nonlinear model fitting with 6 PLDs and 6 averages are the ground truth references. The reported subject has been selected due to the longest mean ATT among three test subjects, which is more challenging to estimate ATT and CBF in practice.

Table 1
Time Saving by Selected PLDs or Averages for H-CNN

Selected PLDs	Time Saving (Total Scan Time)
6 PLDs (all)	0 % (5m 21s)
5 PLDs (1, 2, 3, 5, 6th)	17.80 % (4m 24s)
4 PLDs (1, 3, 4, 5th)	35.60 % (3m 27s)
3 PLDs (1, 4, 5th)	51.14 % (2m 37s)
2 PLDs (1, 4th)	71.21% (1m 32s)

Number of Averages	Time Saving (Total Scan Time)
6	0 % (5m 21s)
5	16.67 % (4m 28s)
4	33.33 % (3m 24s)
3	50.00 % (2m 41s)
2	66.67 % (1m 47s)
1	83.33 % (53s)

Table 1. Total scan time reduction by the reduced numbers of PLDs or averages for the H-CNN.

Title: Calibration and validation of a real-time oximeter for FLASH-RT experiments

Author List: Kaitlyn Liang, Byunghang Ha, Cheng Liu, Rakesh Manjappa, Stavros Melemenidis, Jianghong Rao, Billy W. Loo Jr., and Guillem Pratx

Purpose: To develop real-time optical oximetry under FLASH radiotherapy (FLASH-RT) and conventional radiotherapy, and further understand the normal tissue-sparing effect of FLASH-RT.

Methods: An epifluorescent laser system was constructed to measure the kinetics of O_2 depletion during FLASH-RT with high temporal resolution. A 1 kHz 640 nm laser excites air-tight samples of PBS buffer containing a soluble oxygen-sensitive phosphorescent nanoprobe and various concentrations of oxygen. The same optic fibre detects the 794 nm phosphorescent decay of the nanoprobe. The decay lifetime is calculated by averaging the decays of several pulses, and fitting the data to a dual-exponential function. Calibration measurements with unirradiated samples ranging from 0-100 μM $[O]$ are used to determine the relationship between $[O]$ and probe lifetime (via a Stern-Volmer plot). Validation of this method includes comparing the calculated and known $[O]$ of the calibration samples. Approximately 20 Gy of CONV-RT and FLASH-RT are then repeatedly delivered to separate samples to detect the change in oxygen concentration.

Results: Examination of $[O_2]$ under CONV-RT exhibited a linear decrease in concentration over time during irradiation. The measured O_2 depletion yield agrees with previous measurements made using a polarographic electrode. Under FLASH-RT, $[O]$ exhibited a significantly steeper decrease during irradiation, and an overall 43% +/- 40% smaller yield of depletion. The error bars are absolute, and represent the 95% confidence intervals. To achieve better temporal resolution, a smaller number of decays are combined resulting in significantly wider confidence intervals and decreased SNR. Due to the properties of the nanoprobe, the rate of depletion is most accurately measured when $[O]$ is below 40 μM .

Conclusion: This work supports the potential to measure oxygen levels during FLASH irradiation in-vivo. A greater biochemical understanding of FLASH-RT would be crucial to effective translation of this new treatment to clinical use.

Innovation/Impact: The study is innovative because the instrument and its calibration will allow in vivo oxygen measurements to be conducted before, during and immediately after FLASH-RT, which will help elucidate the role of oxygen depletion in relation to the tissue-sparing effects of FLASH-RT. The designed apparatus will be useful for in-vivo measurements due to the high time resolution, and ability to detect small changes in $[O_2]$.

Key Results: 7 calibration measurements were completed to determine the relationship between nanoprobe lifetime and $[O_2]$. A quadratic term was added to the Stern-Volmer relationship to achieve a suitable fit ($R^2=0.99$; Fig. 1). Two doses of CONV-RT (~20 Gy at 0.186 Gy/s) were delivered consecutively on a sample containing the nanoprobe (Fig. 2 and 3). In this experiment, 50 phosphorescent decays were averaged for each lifetime measurement. Next, 3 doses of FLASH-RT (~20 Gy at 94.74 Gy/s) were performed on a different sample (Fig. 4,5, and 6), where 10 decays were averaged for each measurement. The rate of depletion (ROD) was calculated for both runs (shown in Table 1), indicating that the rate of O_2 depletion is 43% +/- 40% lower during FLASH-RT compared to CONV-RT. The error bars are absolute, and represent the 95% confidence interval.

Table 1: Initial $[O_2]$, Difference in $[O_2]$, and ROD for all CONV-RT and FLASH-RT Runs

Run	Initial $[O_2]$ [μM]	Difference in $[O_2]$ [μM]	ROD [$\mu M/Gy$]
CONV-RT Run 1	90 +/- 2	13 +/- 3	0.65 +/- 0.15
CONV-RT Run 2	74 +/- 1	13 +/- 2	0.65 +/- 0.1
FLASH-RT Run 1	91 +/-4	7 +/- 5	0.35 +/- 0.25
FLASH-RT Run 2	87 +/- 3	7 +/- 4	0.35 +/- 0.2
FLASH-RT Run 3	81 +/-3	8 +/- 4	0.4 +/- 0.2

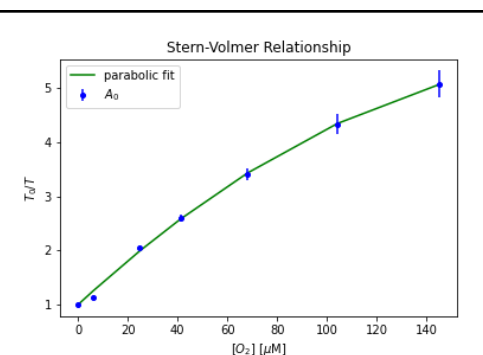


Fig. 1: Stern-Volmer Plot to determine the relationship between probe lifetime and oxygen concentration based on calibration data

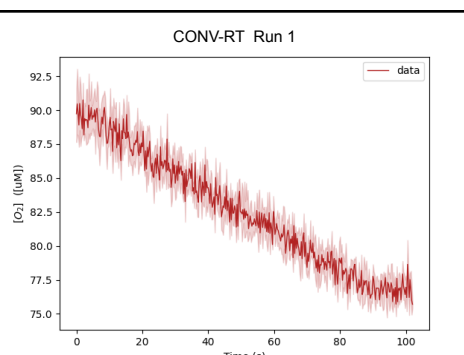


Fig. 2: CONV-RT Run 1 where 20.8 Gy was delivered at 0.186 Gy/s

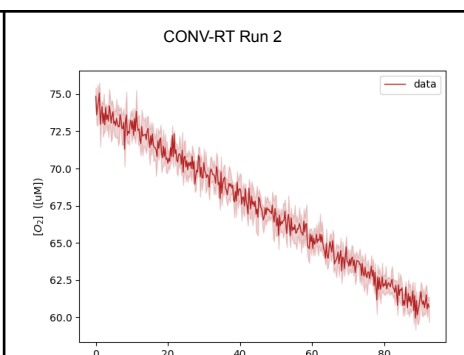


Fig. 3: CONV-RT Run 2 where 21.4 Gy was delivered at 0.186 Gy/s

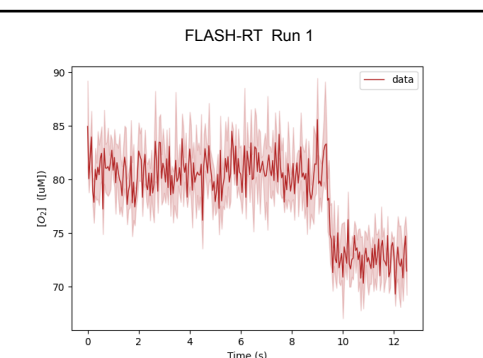


Fig. 4: FLASH-RT Run 1 where 20.89 Gy was delivered at 94.74 Gy/s.

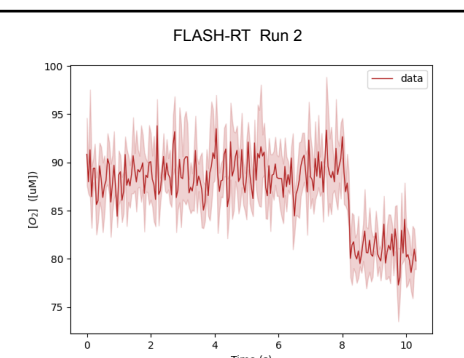


Fig. 5: FLASH-RT Run 2 where 20.39 Gy was delivered at 94.74 Gy/s

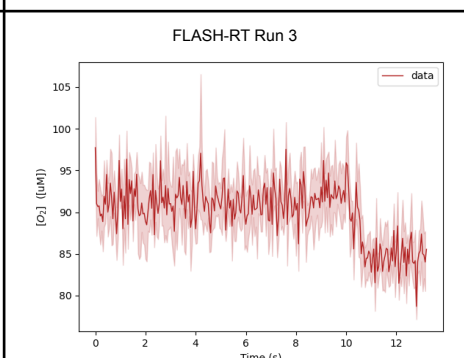


Fig. 6: FLASH-RT Run 3 where 20.61 Gy was delivered. at 94.74 Gy/s

Title: Enabling High Sensitivity and Resolution with Optimized Broadband Receive Front End Design for Magnetic Particle Imaging, Spectroscopy, and Relaxometry

Intro: Magnetic particle imaging (MPI) is a tracer imaging modality that detects superparamagnetic iron oxide nanoparticles (SPIOs). Since its inception [1], MPI has enjoyed a rich developmental history - from its k-space and x-space formulation [2], [3]; to scanner design [4]–[7]; to optimized coil and instrumentation [8]–[11]. Promising clinical applications for MPI include brain imaging [6], [7], [12]; stem cell tracking [13], [14]; immune cell tracking [15]; lung imaging [16]; gastrointestinal bleed imaging [17]; and cancer imaging [18]. Magnetic Particle Spectroscopy (MPS) and Magnetic Particle Relaxometry (MRX) are used to characterize the nanoparticles used in MPI, as well as other biosensing applications [19].

Preclinical MPI, while both highly sensitive and quantitative [citation], has yet to have the resolution for economical human-scale clinical scanner [12], [20]. Novel tracers called Superferromagnetic Iron Oxide (SFMIO) particles show an order-of-magnitude improvement in resolution that would allow for 100-fold decrease in scanner prices. However, these high-resolution tracers show a rich harmonic spectrum showing strong peaks at harmonic numbers well past where common MPI tracers (e.g. VivoTrax/ferucarbotran) have signal above the noise floor, shown in Figure 1 [21]. **Therefore, an order of magnitude improvement in resolution with SFMIOs necessitates a corresponding increase in the RX signal bandwidth.**

This work focuses on optimizing the RX frontend of MPI/MPS/MRX systems to realize this 10-fold increase in bandwidth, while also **improving the limit of detection** with broadband noise matching and **improving dynamic range** with a combination of gradiometric cancellation and active compensation of the drive field feedthrough interference.

Methods: Previous work in MPI broadband noise matching has shown exquisite noise performance down to 100 pV/rtHz voltage noise [9], [10]. However, increasing the noise matching ratio N leads to decreasing effective noise bandwidth due to two major factors. The first is that the resonant frequency of the RX coil decreases as the effective inductance increases (winding more turns or using a transformer increases inductance and capacitance) and effective capacitance increases (adding more amplifiers in parallel increases contribution of input capacitance). Reported resonance frequencies of 200 kHz to 300 kHz, which allows for sufficient bandwidth to reconstruct 10-15 harmonics for VivoTrax and other commercial particles but would squander the several remaining harmonics of SFMIOs. The current noise contribution of the preamplifier due to the increasing impedance of the inductive coil over frequency can also become more dominant than the coil noise voltage and noise voltage of the preamplifier. These two factors limit effective noise match bandwidth. This work showcases a design procedure for minimizing RX noise over a desired bandwidth and improve limit-of-detection, with results in Figure 2.

Drive field feedthrough interference occurs because of transmit (TX) coil to RX coil coupling. Dynamic range suffers when feedthrough interference is too large since the feedthrough may saturate the RX amplifier before the particle signal is adequately amplified. Previous works have used coil geometry to cancel out the interference by reducing the effective mutual inductance between the TX and RX coils [8], [22], [23]. Previous works have also used active components to analog subtract the feedthrough [11], [24], [25]. These techniques achieve several orders of magnitude more suppression for single tone excitation. This work utilizes this concept for broadband suppression with a combination of an easily

shim-able gradiometer for passive compensation and instrumentation amplifier and DAC for active compensation, with results in Figure 3.

With an established noise floor and adequate drive field feedthrough suppression, the next design step is to choose an appropriate Analog-to-Digital Converter (ADC) to quantize the particle signal outlined in the supplementary.

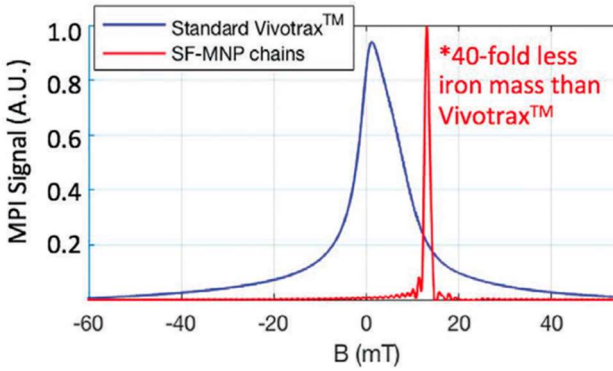


Fig 1A

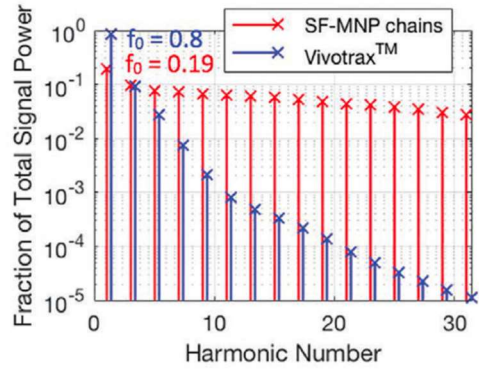


Fig 1B

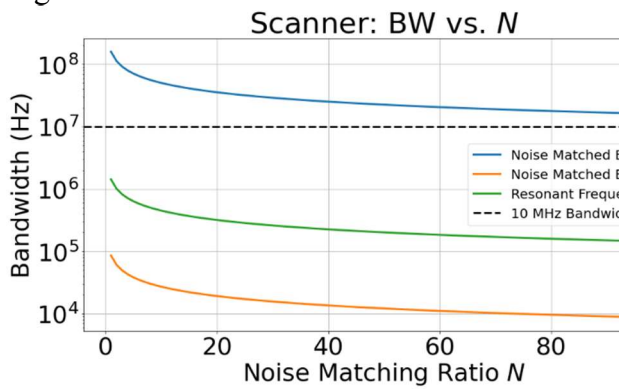


Fig 2A

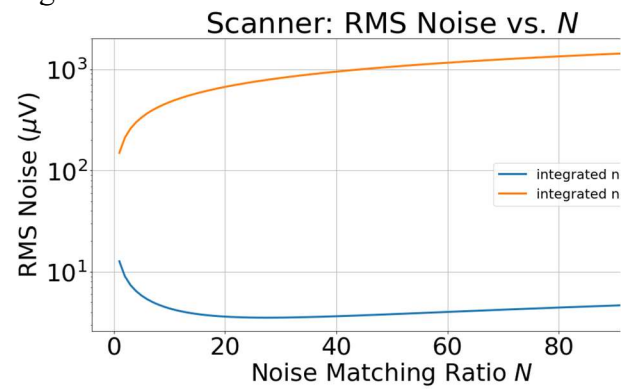


Fig 2B

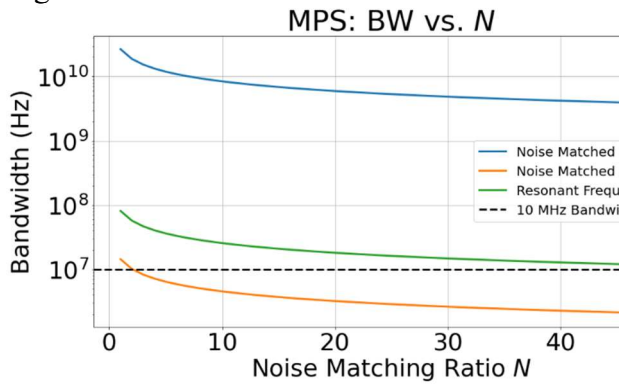


Fig 2C

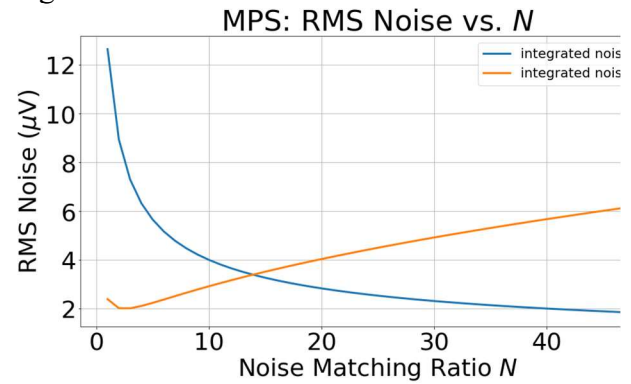


Fig 2D

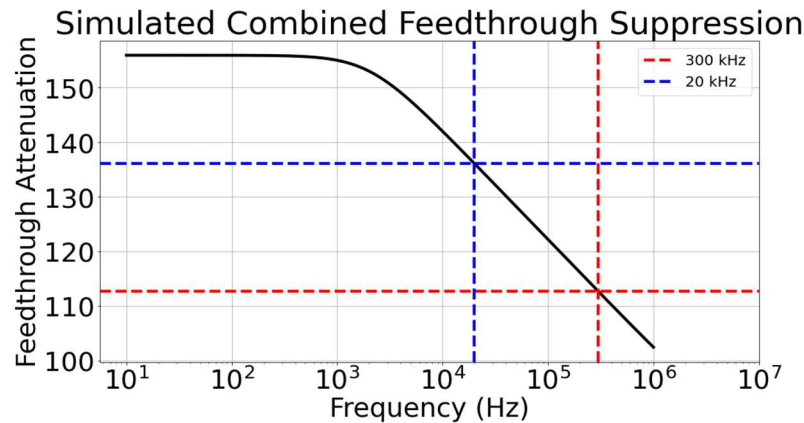


Fig 3

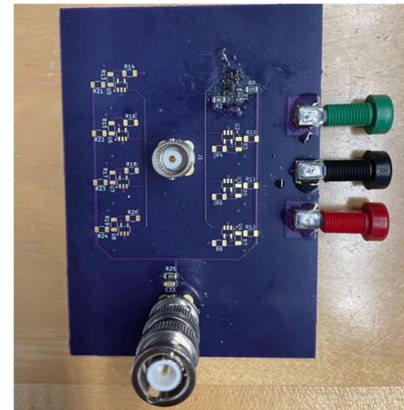
Figure 1: A) Point Spread Function (PSF) of High Resolution SFMIO tracer vs. Vivotrax show much lower Full Width Half Max (FWHM) spatial resolution. B) This potential for sharper resolution is followed by improved harmonic spectra, requiring a much larger RX bandwidth.

Figure 2: A) The bandwidth limiting factor of a MPI scanner with a large inductance RX coil (500 uH) is resonant frequency if using JFET preamplifier. The JFET preamplifier used in this work is SR560 (Stanford Research Systems) and the BJT preamplifier used is LMH6629 (Texas Instruments). B) The integrated rms voltage noise as a function of noise matching ratio. For a scanner sized coil, the best topology is a JFET frontend. C) The bandwidth limiting factor of an MPS/MRX system with low inductance RX coil (3 uH) is current noise if using BJT. However, the integrated rms voltage noise is lower for BJT compared to JFET with lower noise matching ratio.

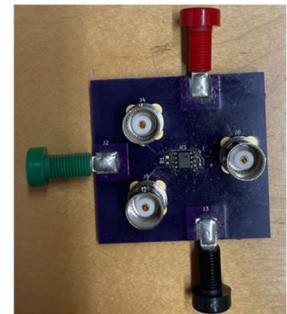
Figure 3: Passive compensation and active compensation are additive. Gradiometric cancellation usually yields 66 dB of broadband cancellation while cancellation with an instrumentation amplifier as an analog subtractor is dependent on the amplifier's common mode rejection if feeding in the feedthrough as a common mode signal. Simulation results (using LTSPICE, Analog Devices) show up to 110 dB suppression over 300 kHz, the bandwidth of the drive field power amplifier used in this work (AE Techron 7224).

Supplementary:

Broadband RX Design Procedure: Two topologies for preamplifiers lend to optimal design choices depending on the RX coil inductance and required bandwidth: JFET frontend amplifiers tend to have larger noise voltage, very small current noise (fA/rtHz), and higher input capacitance while BJT frontend amplifiers have lower voltage noise but much higher current noise pA/rtHz . Figures 1A and 1B show the bandwidth limiting factor of a MPI scanner with a large inductance RX coil and MPS/MRX platform with low inductance RX coil, respectively. After choosing a suitable amplifier, the next step is choosing the optimal noise matching ratio based off the best bandwidth achievable (dominated by resonant frequency or sensor impedance with current noise). In MPI scanners, the receive coil inductance ($500 \mu\text{H}$ in this work) is often $100\times$ larger than that of MPS/MRX systems, suggesting a JFET frontend is more suitable. This causes resonant frequency to be the dominant limiting factor for bandwidth as higher matching ratio N increases (Figure 1A). The MPS/MRX system used in this work has a RX coil inductance of $3 \mu\text{H}$, suggesting a low noise BJT frontend can be more suitable. This causes inductive current noise to be the dominant limiting factor for bandwidth as N increases (Figure 1C). The most important goal to achieve when noise matching is not only maximizing the noise match bandwidth and minimizing noise figure, but ultimately minimizing overall integrated noise. (Figure 1B and 1D). A preliminary design with 8 parallel amplifiers is shown above.



Feedthrough Compensation Design: Gradiometric coil design is outlined in [22], [23] to achieve passive compensation by reducing mutual inductance between the transmit and receive by winding two coils in anti-series. This can reasonably achieve up to 60 dB cancellation. An active compensation approach is using an instrumentation amplifier and playing back the feedthrough during signal acquisition as common mode, utilizing the instrumentation amplifiers high common mode rejection capability to subtract the feedthrough. This can achieve up to the amplifier's CMRR. A preliminary design with a low noise instrumentation amp is shown to the right.



Preserving signal integrity when quantizing the particle signal requires careful selection of the Data Acquisition (DAQ) module. Assuming that there is sufficient ADC resolution to quantize RX thermal noise, using a combination of passive and active feedthrough cancellation to suppress feedthrough to the least significant bit is adequate. However, high RX bandwidth requires high sampling rate ADCs. To summarize, the design goal was to make sure that: Feedthrough = RX thermal noise = LSB ADC and ADC sampling rate $> 2\text{BW}$, which is 10 MHz in this work.

References:

- [1] B. Gleich and J. Weizenecker, "Tomographic imaging using the nonlinear response of magnetic particles," *Nature*, vol. 435, no. 7046, pp. 1214–7, 2005.
- [2] J. Rahmer, J. Weizenecker, B. Gleich, and J. Borgert, "Signal encoding in magnetic particle imaging: properties of the system function," *BMC Med. Imaging*, vol. 9, p. 4, Apr. 2009.
- [3] P. W. Goodwill and S. M. Conolly, "The X-space formulation of the magnetic particle imaging process: 1-D signal, resolution, bandwidth, SNR, SAR, and magnetostimulation," *IEEE Trans. Med. Imaging*, vol. 29, no. 11, pp. 1851–1859, Nov. 2010.
- [4] P. W. Goodwill, K. Lu, B. Zheng, and S. M. Conolly, "An x-space magnetic particle imaging scanner," *Rev. Sci. Instrum.*, vol. 83, no. 3, p. 33708, Mar. 2012.
- [5] P. W. Goodwill, J. J. Konkle, Bo Zheng, E. U. Saritas, and S. T. Conolly, "Projection X-Space Magnetic Particle Imaging," *IEEE Trans. Med. Imaging*, vol. 31, no. 5, pp. 1076–1085, May 2012.
- [6] E. E. Mason, C. Z. Cooley, S. F. Cauley, M. A. Griswold, S. M. Conolly, and L. L. Wald, "Design analysis of an MPI human functional brain scanner," *Int. J. Magn. Part. imaging*, vol. 3, no. 1, 2017.
- [7] M. Graeser *et al.*, "Human-sized magnetic particle imaging for brain applications," *Nat. Commun.* 2019 101, vol. 10, no. 1, pp. 1–9, Apr. 2019.
- [8] G. Bringout and T. M. Buzug, "Coil Design for Magnetic Particle Imaging: Application for a Preclinical Scanner," *IEEE Trans. Magn.*, vol. 51, no. 2, p. 5100808, Feb. 2015.
- [9] B. Zheng *et al.*, "Optimal Broadband Noise Matching to Inductive Sensors: Application to Magnetic Particle Imaging," *IEEE Trans. Biomed. Circuits Syst.*, vol. 11, no. 5, pp. 1041–1052, Oct. 2017.
- [10] M. Graeser *et al.*, "Towards Picogram Detection of Superparamagnetic Iron-Oxide Particles Using a Gradiometric Receive Coil," *Sci. Reports* 2017 71, vol. 7, no. 1, pp. 1–13, Jul. 2017.
- [11] D. Pantke, N. Holle, A. Mogarkar, M. Straub, and V. Schulz, "Multifrequency magnetic particle imaging enabled by a combined passive and active drive field feed-through compensation approach," *Med. Phys.*, vol. 46, no. 9, p. 4077, Sep. 2019.
- [12] X. L. C. Wu *et al.*, "A Review of Magnetic Particle Imaging and Perspectives on Neuroimaging," *AJNR Am. J. Neuroradiol.*, vol. 40, no. 2, p. 206, Feb. 2019.
- [13] B. Zheng *et al.*, "Magnetic particle imaging tracks the long-term fate of in vivo neural cell implants with high image contrast," *Sci. Rep.*, vol. 5, Sep. 2015.
- [14] B. Zheng *et al.*, "Quantitative Magnetic Particle Imaging Monitors the Transplantation, Biodistribution, and Clearance of Stem Cells In Vivo," *Theranostics*, vol. 6, no. 3, pp. 291–301, 2016.
- [15] P. Chandrasekharan *et al.*, "Non-radioactive and sensitive tracking of neutrophils towards inflammation using antibody functionalized magnetic particle imaging tracers," *Nanotheranostics*, vol. 5, no. 2, p. 240, 2021.
- [16] X. Y. Zhou *et al.*, "First In Vivo Magnetic Particle Imaging of Lung Perfusion in Rats," *Phys. Med.*

Biol., vol. 62, no. 9, p. 3510, Apr. 2017.

- [17] E. Y. Yu *et al.*, "Magnetic Particle Imaging for Highly Sensitive, Quantitative, and Safe in Vivo Gut Bleed Detection in a Murine Model," *ACS Nano*, vol. 11, no. 12, pp. 12067–12076, 2017.
- [18] E. Y. Yu *et al.*, "Magnetic Particle Imaging: A Novel in Vivo Imaging Platform for Cancer Detection," *Nano Lett.*, vol. 17, no. 3, pp. 1648–1654, Mar. 2017.
- [19] Z. W. Tay, P. W. Goodwill, D. W. Hensley, L. A. Taylor, B. Zheng, and S. M. Conolly, "A High-Throughput, Arbitrary-Waveform, MPI Spectrometer and Relaxometer for Comprehensive Magnetic Particle Optimization and Characterization," *Sci. Rep.*, vol. 6, Sep. 2016.
- [20] Z. W. Tay, D. W. Hensley, E. C. Vreeland, B. Zheng, and S. M. Conolly, "The Relaxation Wall: Experimental Limits to Improving MPI Spatial Resolution by Increasing Nanoparticle Core size."
- [21] Z. W. Tay *et al.*, "Superferromagnetic Nanoparticles Enable Order-of-Magnitude Resolution & Sensitivity Gain in Magnetic Particle Imaging," *Small Methods*, vol. 5, no. 11, Nov. 2021.
- [22] A. R. Çağıl, B. Tasdelen, and E. U. Saritas, "Design of a Doubly Tunable Gradiometer Coil," *Int. J. Magn. Part. Imaging*, vol. 6, no. 2 Suppl 1, pp. 1–3, Sep. 2020.
- [23] Q. Huynh *et al.*, "Design of a more easily shimmable gradiometric coil using linear programming," *Int. J. Magn. Part. Imaging*, vol. 8, no. 1 Suppl 1, Mar. 2022.
- [24] T. Q. Bui, W. L. Tew, and S. I. Woods, "AC magnetometry with active stabilization and harmonic suppression for magnetic nanoparticle spectroscopy and thermometry," *J. Appl. Phys.*, vol. 128, no. 22, p. 224901, Dec. 2020.
- [25] B. Tasdelen *et al.*, "Vector Modulator Based Active Compensation of Direct Feedthrough," *Int. J. Magn. Part. Imaging*, vol. 6, no. 2 Suppl 1, pp. 1–3, Sep. 2020.

***In Vivo* therapeutic cell tracking using Magnetic Particle Imaging to optimize solid tumor immunotherapies**

Authors Renesmee Kuo, Barry Fung, Prashant Chandrasekharan, Quincy Huynh, Chinmoy Saayujya, Caylin Colson, Jacob Byran, Kim Hwang Yeo, Benjamin Fellows, Steven Conolly

Motivation Circulating white blood cells (WBCs) find and defend our bodies against both foreign invaders like bacteria and viruses and internal pathologies like tumors. In 2018, James Allison and Tasuku Honjo won the Nobel Prize for immunotherapy, a cancer treatment strategy where a patient's immune system is supercharged to recognize and kill cancer cells. Immunotherapies are already the leading treatments for blood cancers, which account for 10% of all tumors. However, 90% of cancers are solid tumors. Partially due to weak efficacy and risky complications, two leading methods: chimeric antigen receptor (CAR)-T and CAR-NK therapies are yet the preferred treatments for solid tumors [1]. Today's clinical WBC imaging methods are scintigraphy and single-photon emission computed tomography (SPECT), which label a patient's autologous WBCs with either Tc99m or In111. However, T and NK cells die from radiation poisoning before the scan is completed [2,3].

Magnetic Particle Imaging (MPI) is a new biomedical imaging modality that uses superparamagnetic iron oxide (SPIO) tracers to track cells [4-10]. Unlike WBC scintigraphy and SPECT, MPI uses zero radiation and works everywhere in the body. Here, we show the first *in situ* labeling and tracking of neutrophils to the reticuloendothelial system (RES) (liver, spleen and bone marrow), with no damage to cell viability and functionality. MPI could soon quickly and quantitatively assess novel CAR-T and CAR-NK therapies' ability to target tumors with specificity.

Methods Anti-Ly6G-antibody-conjugated SPIOs (Ab-SPIOs) (IgG1, REA526 clone, Miltenyi Biotec, GmbH) were purified using dialysis and injected into healthy mouse models. The biodistribution of tracers were imaged with a 6.3T/m field free line (FFL) MPI scanner (projection FOV 10.6 x 6.2 cm, $t = 95$ s/projection). 3D tomography images were acquired post-euthanasia. Forty 2D projection images were acquired at equally spaced angles and reconstructed using a Radon transformation. All 3D data were re-binned to a voxel dimension of $0.04 \times 0.04 \times 0.034$ cm³. The images were compared with an X-ray image of the mouse [11]. Fluorescence activated cell sorting (FACS) was used to analyze viability of B3Z murine hybridoma T cell expressing receptors (TCR) that specifically recognizes ovalbumin (OVA). A flask of cells was exposed to 5 Gy of radiation, and another had 100 μ L of VivoTrax added to it. The cells were harvested and stained with annexin V-FITC and propidium iodide (PI).

Results Twenty-four hours post-intravenous (IV) injection of anti-Ly6G SPIOs, maximum intensity projection (MIP) MPI images showed tracers binding to neutrophils that home to organs of the RES, including liver, spleen and bone marrow. These results are similar to anti-NCA95-antibody scintigraphy tracers that are traditionally used for neutrophil tracking [12]. FACS analysis showed that the early apoptotic cell population increased from 6% for SPIO-labeled cells to 15% for 5 Gy irradiated cells. Similarly, the necrotic cell population increased from 0.1% for SPIO-labeled cells to 12% for 5 Gy irradiated cells. This result suggests that radiation causes apoptosis in CAR-T cells while SPIOs showed no visible effect on cell viability.

Conclusion The *in vivo* antibody-conjugated SPIOs targeting WBCs highlights MPI's potential to image the immune system. MPI could soon safely and effectively address the pitfalls of scintigraphy and SPECT. Immunotherapy-MPI could help doctors and researchers monitor the success of immunotherapy and diagnose bone marrow disorders and diseases, all without ionizing radiation and with infinite persistence.

References [1] Xu, Jian, et al., *Gene Ther Mol Biol*, 13.1, 2009; [2] D. A. Goodwin., *J Nucl Med*, 19(5), 1978; [3] FDA, *Drugs@FDA*, 2015; [4] Gaudet et al., *Cancer Research*, 2019; [5] Chandrasekharan et al., *Theranostics*, 2020; [6] Makela et al., *Molecular Imaging and Biology*, 2020; [7] Chandrasekharan et al., *Nanotheranostics*, 2021; [8] Rivera-Rodriguez et al., *Nanotheranostics*, (5) 2021 [9] Sehl, Foster, *Scientific Reports*, 2021; [10] Kiru et al., *PNAS*, 2022; [11] Dogdas et al., *Phys Med Biol*, 2007; [12] Agool et al, *Eur J Nucl Med Mol Imaging*, 2011.

Residents

Ramish Ashraf (Stanford)

- **Film-Less Quality Assurance (QA) of a Robotic-Arm Linac Using a Scintillation-Based Imaging System**

Kamal Singhrao (UC Francisco)

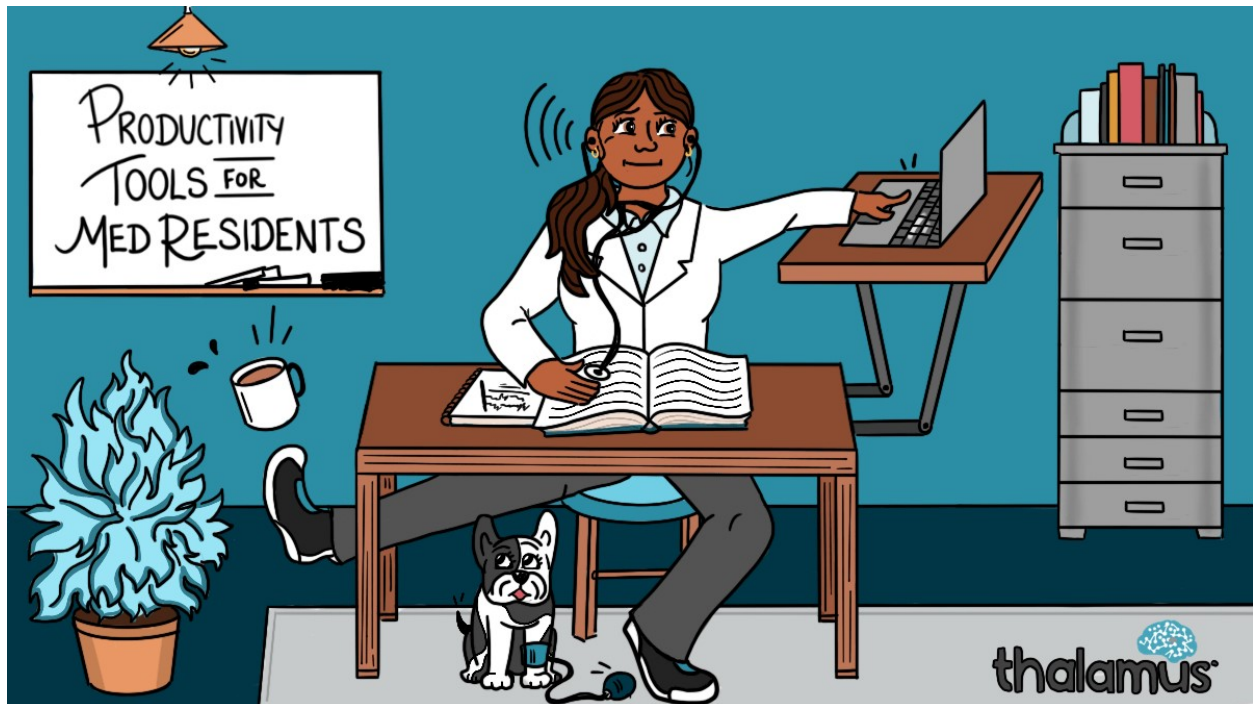
- **Development of Quality Assurance Metrics for Synthetic CT (sCT) Image Generation of Treatments Utilizing MRI-Only Simulation for External Beam Radiotherapy**

Jose Ramos-Mendez (UC Francisco)

- **Towards the employment of nanodosimetric quantities in treatment planning for charged particle radiotherapy**

Meghan Keohane (UC Davis)

- **Comparing spatial accuracy of catheter localization between stepping-transverse mode and twister-sagittal mode in transrectal ultrasound (TRUS) based high-dose-rate (HDR) brachytherapy for prostate cancer**



Film-Less Quality Assurance (QA) of a Robotic-Arm Linac Using a Scintillation-Based Imaging System

Purpose:

To develop and characterize a rapid, low-cost, and high-resolution scintillator-based imaging system for quality assurance (QA) of a robotic arm linear accelerator, which would replace reliance on film dosimetry.

Methods:

An integrated QA phantom was 3D printed which consisted of a scintillating sheet, fiducial markers, a low-cost CMOS camera and a light tight enclosure. The camera, equipped with a 12 mm lens, was angled at 45 degrees with a direct line of sight of the scintillating sheet. The phantom was constructed such that it can be used to image AP and lateral beams. A perspective image transformation with optical distortion correction was then employed to obtain a beam's eye view image. Beams with fixed cones, Iris, and multileaf collimation (MLC) were imaged and compared to gafchromic film. A garden fence pattern constructed using the MLCs were also imaged to verify leaf positioning. The system's sensitivity to changes in output, field size and leaf positioning was also assessed. Finally, a user interface was developed which enabled efficient analysis, making it suitable for routine morning QA.

Results:

The limiting resolution of the optical system defined as the full-width half maximum of the line spread function, was measured to be ~ 0.3 mm. Field size, as measured by the camera-based system for fixed cone and Iris apertures, was within 0.2 mm of the values measured using film. The imaging system was sensitive to output changes as small as 1 Monitor Units (MU). Individual MLC leaves were successfully resolved and the average difference between expected leaf position compared to the optically measured position was 0.11 mm. The optical system was able to detect leaf positioning errors as small as 0.3 mm. Excellent agreement was seen for relative central axis beam profiles for 10 mm and 5 mm Iris collimated beams. Low-energy scatter at the surface led to the optical response being higher outside the projected radiation field when compared to film data, but the effect was minimal for small fields (<10 mm).

Conclusions:

The optical system presented here is a promising low-cost alternative to film and electronic portal-based imaging devices and will obviate the need for cumbersome and time consuming read-out procedure associated with film dosimetry. For the next iteration, the optical system will be adapted to perform end to end and targeting accuracy tests. The system is also an ideal candidate QA for spot-scanned proton beams. The user interface, along with 3D models of the phantom will be made open source.

Supporting Document:

Innovation/Impact: Certain quality assurance checks for Iris and fixed cones are heavily reliant on gafchromic film. Moreover, routine morning QA for MLC is reliant solely on visual verification of MLC leaf positioning on film. Film requires calibration for each batch and has a cumbersome read-out procedure, which, if not performed correctly can lead to significant errors. While certain electronic portal imaging devices are available for Cyberknife, these tend to be costly. The purpose of this study was to build and characterize a QA tool, which can enable rapid verification of fixed cone, Iris and MLC leaf positioning without having to rely on film. After successful characterization and reproducibility tests, we intend to make the 3D model and MATLAB graphical interface easily open source, so that other clinics looking for low-cost solutions can make use of the system proposed here.

Key Results: Initial characterization and development of the system is presented in Figure 1-4. Figure 1 shows the general imaging setup and the 3D model of the phantom. Figure 2 presents comparison of beam profiles for different Iris apertures between film and optical setup. While blurring was seen in the penumbra region, excellent agreement was seen for small fields, indicating minimal volume averaging. Figure 3 presents preliminary results for MLC QA. Individual leaves can be resolved. Next steps would entail testing the sensitivity of the system against misalignment of MLC leaf positioning and Iris aperture misalignment. Figure 4 presents results for the field size QA. Excellent agreement (<0.1mm on average) was seen for field size verification, which validates the use of this device for routine daily QA.

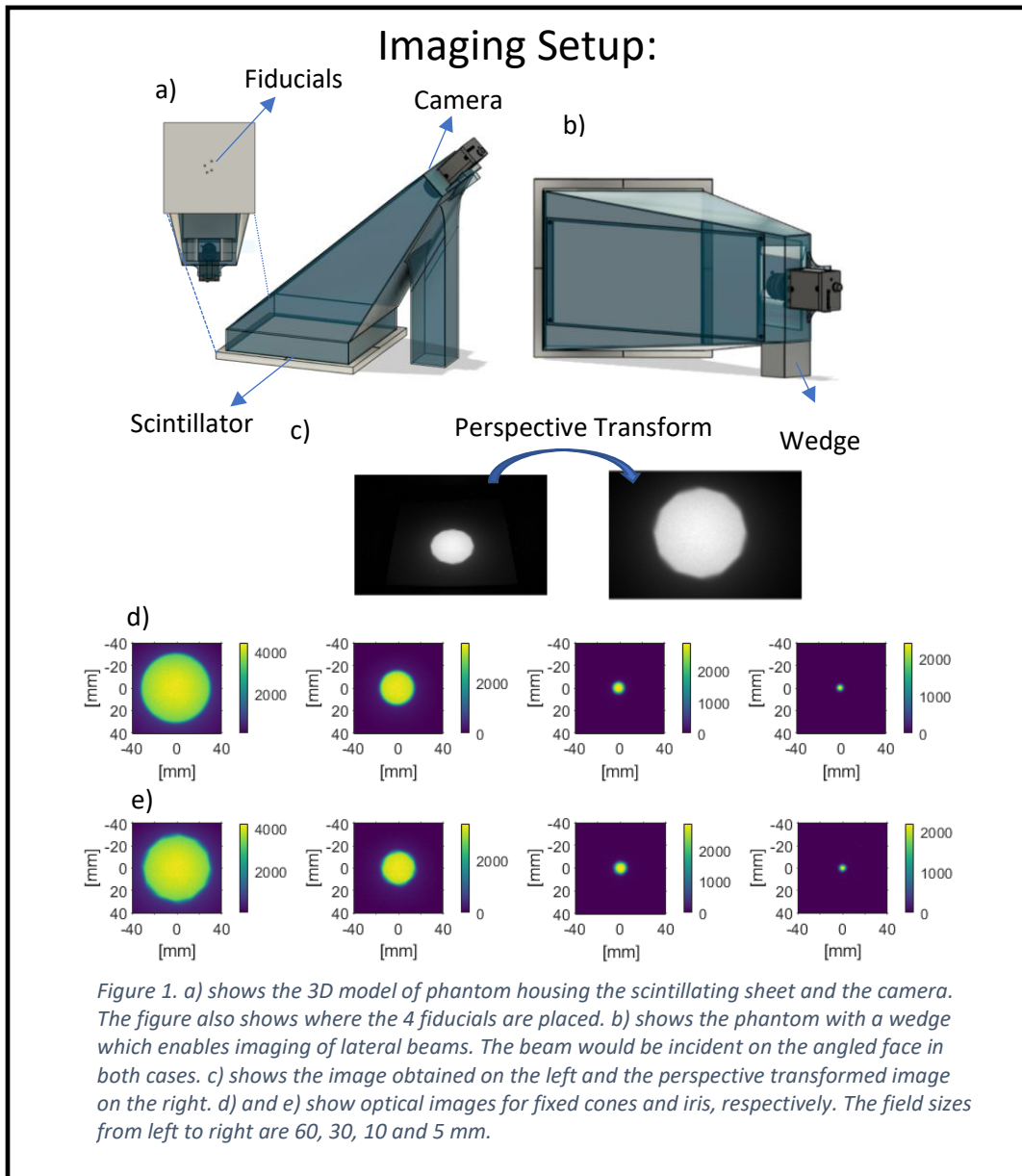
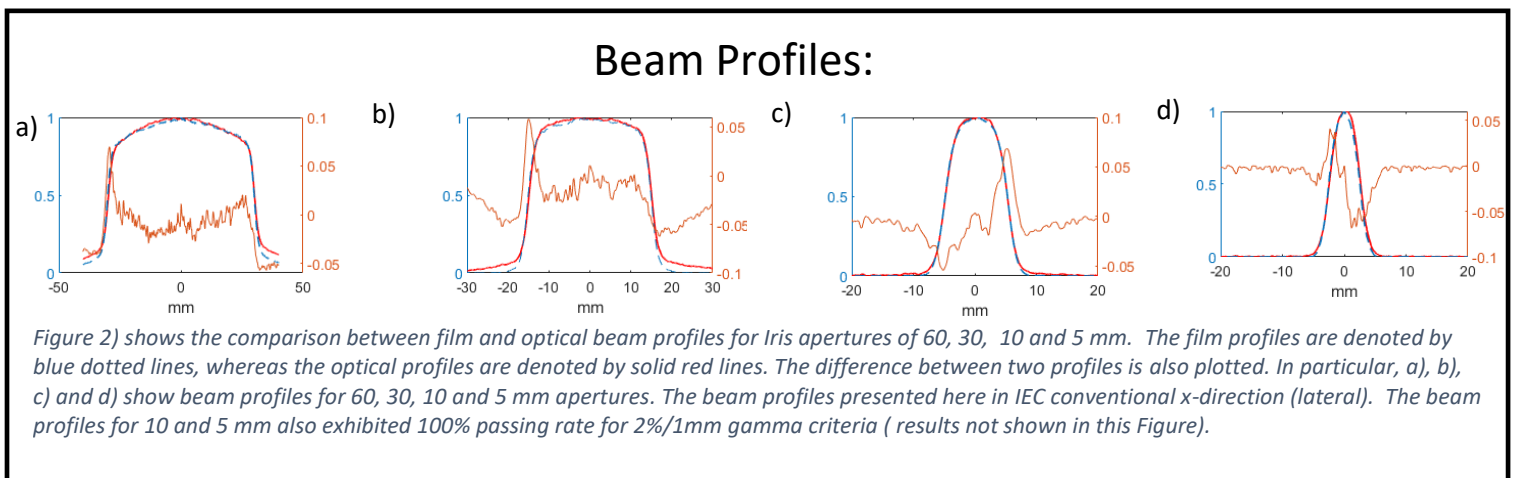


Figure 1. a) shows the 3D model of phantom housing the scintillating sheet and the camera. The figure also shows where the 4 fiducials are placed. b) shows the phantom with a wedge which enables imaging of lateral beams. The beam would be incident on the angled face in both cases. c) shows the image obtained on the left and the perspective transformed image on the right. d) and e) show optical images for fixed cones and iris, respectively. The field sizes from left to right are 60, 30, 10 and 5 mm.



MLC QA:

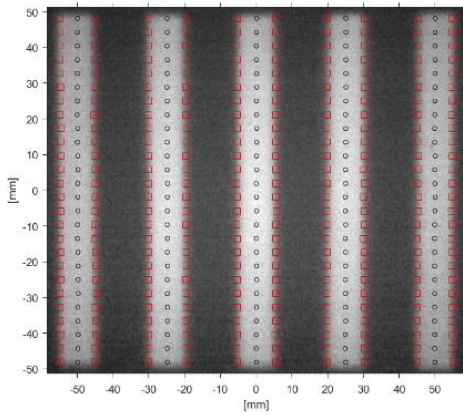


Figure 3) a) shows the garden fence pattern as imaged by the camera-based system. The individual leaf pairs were identified by identifying peaks in the intensity profiles. The intensity profiles were rescaled in intensity, and zero crossing points were identified (indicated by red squares in the image). The center of the leaf pairs (indicated by black circles in the image) were identified by averaging the two zero crossing points

Field Size QA:

Diameter (mm)	Film Avg Field Size (mm)	Optical Avg Field Size (mm)	Difference (mm)
60	61.85	61.67	0.18
30	30.60	30.60	0
10	9.88	9.84	0.04
5	4.80	4.84	0.04

Diameter (mm)	Film Avg Field Size (mm)	Optical Avg Field Size (mm)	Difference (mm)
60	59.48	59.59	0.1
30	29.96	30.03	0.07
10	10.22	10.22	0
5	5.04	5.13	0.09

Figure 4) Field size comparison of film against optical imaging is presented for fixed cone and Iris. The average field diameter was determined by taking an average of 12 profiles as shown below in Figure 5.

User Interface:

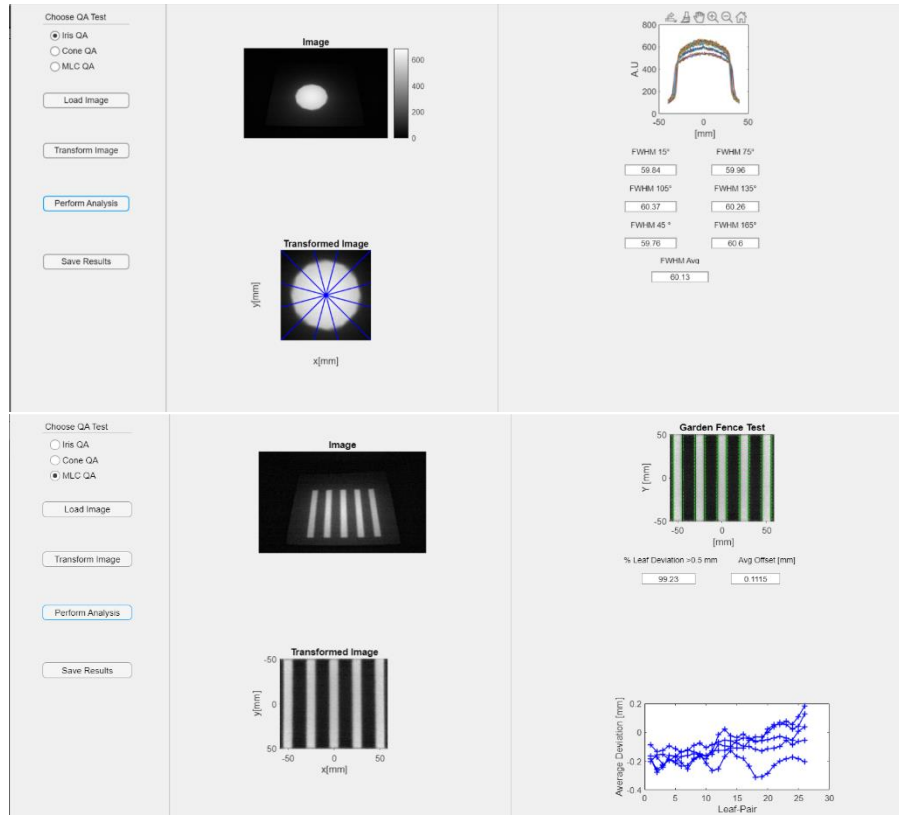


Figure 5) This figure shows the user interface depicting analysis for MLC and Iris collimator. For iris collimator, field size is determined by averaging radial profiles every 12 degrees. The results are saved in a excel file. Future work on the user interface would include a trend analysis, where users can see the variation in QA results from baseline.

Title: Development of Quality Assurance Metrics for Synthetic CT (sCT) Image Generation of Treatments Utilizing MRI-Only Simulation for External Beam Radiotherapy

Purpose: MRI-only radiotherapy simulation can provide numerous clinical benefits including improvements in target delineation, reduction in treatment-planning induced uncertainties and reduction in patient load. Synthetic CT (sCT) images are generated as part of the MRI-only planning workflow to provide electron densities for dose calculations and for patient setup. A major challenge to the clinical implementation of MRI-only radiotherapy planning is quality-assurance (QA) of sCT images. Current methods for QA of MRI-only workflows require the acquisition of an additional CT scan which increases patient load and potentially reintroduces image registration errors during planning. In this study, we produced QA criterion for clinical acceptability of sCT images by correlating image similarity metrics to dosimetry and alignment errors using only MRI-simulation and their corresponding sCT images.

Methods/Materials: MRI-simulation images from 5 pelvic cancer patients were included in this study. Bulk-density (BD) and deep-learning (DL) model-based sCT images were generated using two commercially available sCT methods. Criteria for clinical acceptability was correlated using MRI/sCT image correlation scores and dosimetry/alignment errors after adding artifacts into each sCT. To emulate artifacts commonly seen in MRI-based sCT generation, bone and air artifacts of varying volumes were inserted into different parts of sCT images. Over 400 corrupted sCT images were generated for each patient containing bone/air artifacts. Mutual information (MI) and structural-similarity-index-metric (SSIM) were calculated as proxies for the MRI/sCT image similarity. A 5-field intensity-modulated-radiation-therapy (IMRT) prostate plan was created using the original sCT image and doses were recalculated onto corresponding corrupted sCTs. sCT vs corrupted sCT gamma indices and mean planned dose-differences were reported. MRI/sCT image translational errors are reported for each corrupted sCT.

Results: SSIM and normalized-MI scores that resulted in a planned-dose-difference below 2% and local gamma-index (2%/2mm/10% threshold) below 98% were 0.996 (bone-artifacts) (BD-method) and 0.995 (bone-artifacts) (DL-method), and 0.994 (bone/air artifacts) (BD-method) and 0.993 (bone/air artifacts) (DL-method), respectively. Root-mean-square translational alignment differences for all tested corrupted sCT images were below 2mm.

Conclusions: This work has demonstrated the proof-of-concept that image similarity metrics can be used to provide clinical endpoint-based quality assurance metrics to allow for evaluation of sCT images produced using only MRI-simulation images. Future work will involve including additional patient statistics, addition of more sCT generation methods and the inclusion of other clinical sites such as head/neck.

Innovation/Impact: Magnetic resonance imaging- (MRI)-only simulation can bring benefits to the radiotherapy workflow because the modality produces images with excellent soft tissue contrast. This could potentially allow for better target/organ-at-risk delineation and increase contouring consensus, which can in turn decrease planning margins. However, a fundamental problem with MRI-only workflows is the step required to generate synthetic computed tomography (sCT) images does not have an independent quality assurance (QA) check. sCT generation methods can generate errors such as misassigning voxels or objects as bone or air, and in a worst-case scenario, could potentially impact dosimetry and alignment [1,2]. The manual validation of sCT errors typically falls on treatment planning teams. There is no clear consensus on what types of random errors in sCTs are deemed unacceptable or could compromise patient dosimetry and setup. Previous studies have used deformed reference computed tomography (CT) images to evaluate errors in sCT images. However, a true MRI-only simulation workflow cannot rely on CT image validation since they are not acquired. In this study we develop a framework to correlate image similarity metrics, structural similarity index metric (SSIM) and mutual information (MI), using only MRI and sCT images, to dosimetric and alignment errors with increasingly corrupted sCT images. Artifacts were simulated using structuring elements that moved around each sCT image with varying volumes. Bone/air artifacts were simulated by overriding the density of the artifact to 10000/-1000 HU respectively. We tested an FDA-cleared bulk density method (Siemens, Erlangen, Germany) and a CE-marker/FDA-approval-pending deep-learning based sCT generator (Spectronics Medical, Sweden).

Key Results: **Figure 1** shows a parent MRI, corresponding sCT and corrupted sCT images with the bone and air artifacts introduced. The dosimetry study involved creating over 1000 corrupted sCTs across 5 patients who received MRI scans to generate sCTs using one or both bulk-density/deep-learning methods. A sample 5 field pelvis external beam radiotherapy plan was created using MatRad [3] and doses were recalculated on each sCT image (**Figure 2**). The effect

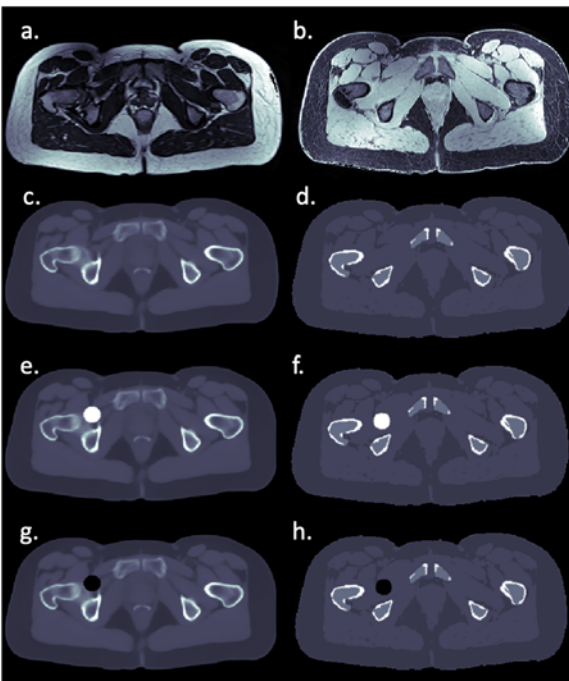


Figure 1: Axial images of bias corrected (a) 3D T2 weighted spin echo and (b) DIXON VIBE MRI and their corresponding (c) deep-learning, (d) bulk-density sCT images. An example of a sCT corruption is shown with an artificially added bone (e,f) and (g,h) air artifacts are shown.

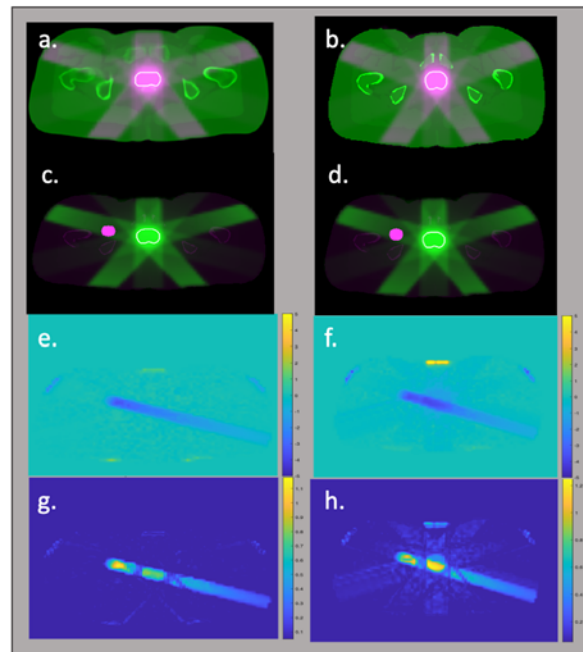


Figure 2: A 5 field IMRT plan was created for a clinical target for each sCT image set. Fluence optimization was performed on the uncorrupted (a) bulk-density and (b) deep learning sCT image. Doses were recalculated on each corrupted sCT image (c,d) (example bone artifact shown in pink). % dose differences and gamma index maps between doses calculated on uncorrupted/corrupted sCTs are shown in (e,f) and (g,h) respectively.

of artifact-based degradation on dosimetry metrics (gamma/%dose difference/artifact volume) vs image quality metrics (MI and SSIM) is shown in **Figure 3** which shows data for a single sample patient who had either a bulk-density or deep-learning based sCT generated. A global fit for all the data (based on 1000 corrupted sCTs for bone and air respectively) is overlaid for each plot. Multimodal image registration was used to register the parent MRI and (corrupted and uncorrupted) sCT images. **Table 1** shows the mean alignment error from across all corrupted sCT images used in the study. Based on the data from **Table 1** for corruptions of the volumes used in this study did not induce an alignment error greater than 2mm across both sCT image types tested.

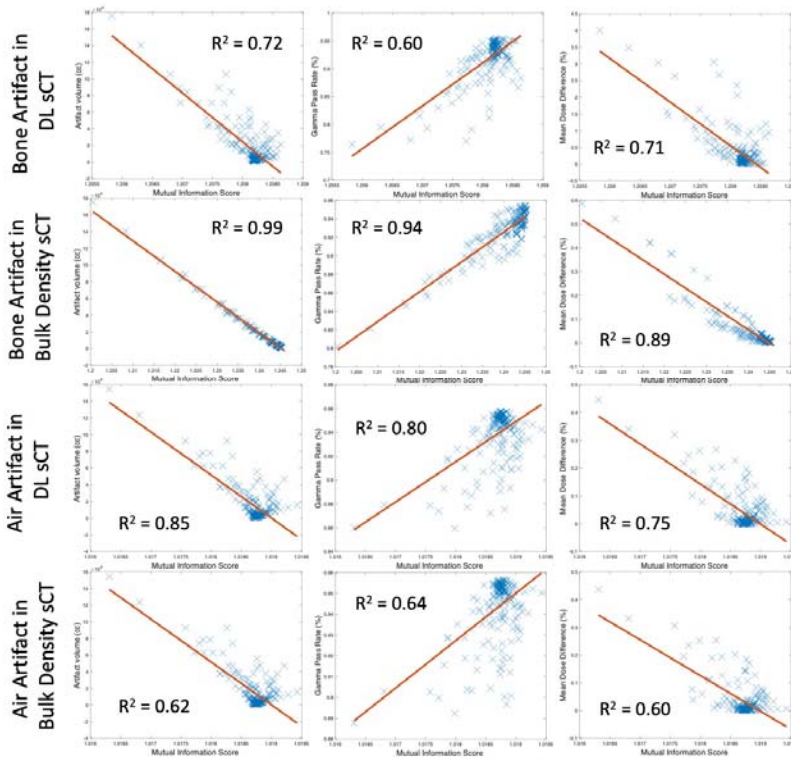


Figure 3. Data from a sample patient showing the mutual information scores vs artifact volume, mean planned dose differences and gamma indices for bone and air artifacts introduced into bulk-density and deep-learning sCT images. Fit models are based on the aggregate data and overlaid over this single patients data to show the correlation between mutual information and artifact errors.

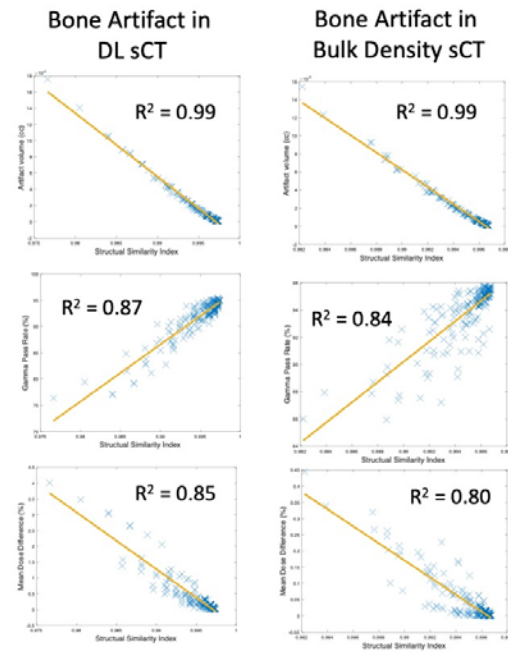


Figure 4. Data from a sample patient showing the structural similarity index vs artifact volume, mean planned dose differences and gamma indices for bone and air artifacts introduced into bulk-density and deep-learning sCT images. Fit models are based on the aggregate data and overlaid over this single patients data to show the correlation between mutual information and artifact errors.

MRI-sCT registration error	Bone corruptions (bulk density)	Air corruptions (bulk density)	Bone corruptions (deep-learning)	Air corruptions (deep-learning)
3D error (mm)	2.0 ± 1.0	1.2 ± 0.6	1.1 ± 0.5	1.4 ± 0.6

Table 1. Root-mean-square translational errors based on multimodal image registration between MRI-sCT, for sCT images for all the corruptions tested in this study. Results are reported for bone and air corruption artifacts in bulk density and deep-learning sCT images are reported.

- [1] Gupta D, Kim M et al, Front. Oncol., Sept 2019
- [2] Farjam et al, *J Appl Clin Med Phys*, 2019
- [3] Wieser HP, et al. Med Phys. 2017;44

Towards the employment of nanodosimetric quantities in treatment planning for charged particle radiotherapy.

Purpose: To propose a model for the application of the detailed spatial distribution of ionization along a particle track, to proton and ion beam radiotherapy treatment planning (RTP).

Methods: It is shown that the model relate nanoscopic parameters of ionizing radiation to biological effects in proton and ion beam therapy. To that end two different parameters calculated using Monte Carlo track structure simulations are presented. One, N_2 , is the number of ionizations clustered in small targets where at least two ionizations per particle were produced. The other, F_4 , is the number of clusters of four or more ionizations per particle track. Then it is demonstrated its correlation with published data on cell inactivation under aerobic and hypoxic conditions with carbon, argon and neon ions, covering a wide range of linear energy transfer (LET). Finally, it is shown how the model may be applied to nanoscopic-based RTP. For that, the quantity mass cluster size density is proposed to provide the means to bridge the large gap between nanoscopic ionization structure and macroscopic RTP.

Results: Considering different ion beams with the same fluence, the cell survival was sensitive to the particle type for beams having the same LET or N_2 . On the other hand, for beams having the same F_4 , the aerobic cell survival was insensitive to the particle type. Based on these results, it is reasonable to assert that there exist nanodosimetric parameters that are more closely associated with biological effects than current LET-based approaches used in particle RTP.

Significance: Our model provides a practical means to employ the knowledge of the physical structure of ionization along particle tracks obtained at the nanometer scale to RTP at the millimeter scale.

Status: Medical Physics Resident

Title: Comparing spatial accuracy of catheter localization between stepping-transverse mode and twister-sagittal mode in transrectal ultrasound (TRUS) based high-dose-rate (HDR) brachytherapy for prostate cancer

Authors: Megan Keohane, Sonja Dieterich, Jason Matney, Patrick Beagen, Jason Zhao, Richard Valicenti, Tian Liu, Stanley Benedict, Peter Park.

Abstract

Purpose: The objective of this study was to measure and compare spatial accuracy of the catheter in TRUS volume images acquired in transverse mode and sagittal mode using computed tomography (CT) as the baseline.

Methods: Three aftermarket tissue-mimicking phantoms that consist of the prostate, urethra, and rectum anatomy were used for this study. A TRUS stepper with a catheter guiding grid system was set up on a CT table similar to the clinical setup. An ultrasound probe was used to scan the phantoms in both stepping-transverse mode and twister-sagittal mode before and after insertion of catheters with a pre-defined pattern. Immediately after the TRUS acquisition, CT images were acquired with the locked grid holding the catheters in the same position. Both ultrasound sound images were registered to their respective CT image based on the prostate and rectum surface. In transverse view, the center coordinate of the catheter in the CT (seen as a hypo-dense circle) and the center of echoes (seen as a hyper-echoic line) for ultrasound images was recorded. In sagittal and coronal views, the bevel of the catheter was identified and recorded in both ultrasound images and the reference CT. The bevel location served as the catheter depth in the phantom. A total of 26 catheters were analyzed. For each cartesian direction, spatial accuracy was compared between stepping-transverse mode and twister-sagittal mode using paired t-test.

Results: The mean difference of spatial accuracy between the two modes were 1.27, -0.07, and 1.23 [mm] for left-right, ant-post, and in-depth respectively. Both left-right and in-depth direction showed statistically significant difference ($p < 0.05$).

Conclusions: Volume image acquired using twister-sagittal mode produced a larger error in the left-right direction. In both modes, the center of the catheter identified using CT was on average 2.35 [mm] radially above the hyper-echoic line visualized in ultrasound images.

Naoki Dominguez Kondo (UC Francisco)

- **Monte Carlo Track-Structure study of DNA damage in supercoiled plasmids.**

Yansong Zhu (UC Davis)

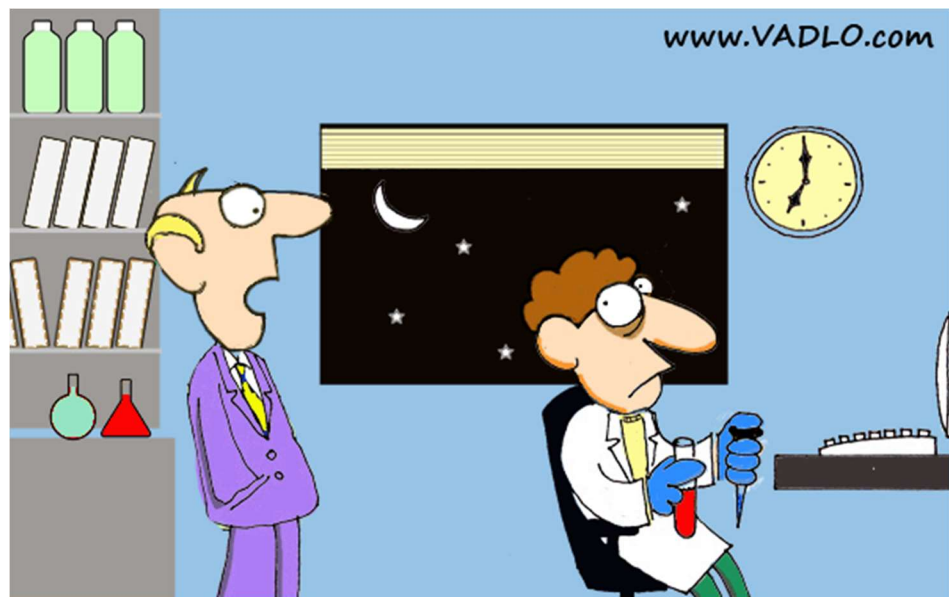
- **Simultaneous estimation of blood input function using a kernel method and its evaluation with total-body PET**

Reimund Bayerlein (UC Davis)

- **Qualitative and Quantitative Validation of a Scatter Correction Method for Total-Body Positron Emission Tomography**

Shengtian Sang (Stanford)

- **A Cross-Attention Method Based on Tumor-Feature-Templates for Segmenting Small Liver Tumors in CT Scans**



“Just work till midnight, you need to relax too”

Monte Carlo Track-Structure study of DNA damage in supercoiled plasmids.

Background And Purpose

The quantification of the biological effect of modern radiotherapy is built on top of phenomenological models whose parameter tuning is driven by experimental measurements. Improvement of such models requires understanding of the mechanisms of DNA damage at the macro and nano scale. Monte Carlo Track-Structure simulations (MCTS), provides sufficient special resolution to identify possible factors that involves the interaction of ionizing radiation with DNA structures, creating a synergy between experiments and modeling that leads to the observable effects. In this work, we developed the tools needed to perform MCTS of DNA strand-breaks in supercoiled DNA plasmids considering the physical and chemical contributions of ionizing radiation at low LET radiation using TOPAS-nBio.

Methods

With the developed tools we performed simulations to estimate the response of irradiated DNA under realistic experimental conditions. These conditions included temperature, •OH scavenging capacity, DNA concentration, DNA compactness and absorbed dose. DNA single- and double-strand breaks were reported for pUC19 supercoiled plasmids irradiated by cobalt and cesium gamma rays. Simulation results were compared with experimental data from the literature.

Results

The simulated results recreated the experimental behavior for DNA strand breaks (SBs) within one standard deviation. Results showed an increase of the number of SBs of 100% between 0-46 °C; a ten-fold increase between 5.62-100.12 $\mu\text{g ml}^{-1}$ of DNA concentration; 4.5% increase between -0.06 and -0.03 super helix density; and 5.2-fold between 20-125 Gy of absorbed dose. As a function of the •OH scavenging capacity, a decrease of 2500-fold was estimated between 1×10^{-4} -1 M of scavenger concentration. Finally, the efficiency of DNA SBs induced by •OH radicals was estimated as 13.8%, in agreement with measured data.

Conclusions

We showed that simulations with TOPAS-nBio are capable of recreating experimental results with good accuracy, making them a viable resource for further studies regarding quantities of interest for radiobiology.

Simultaneous estimation of blood input function using a kernel method and its evaluation with total-body PET

Yansong Zhu, Post-doc from UC Davis, Department of Radiology
Advisor: Guobao Wang

Purpose :

Dynamic PET allows quantification of physiological parameters through kinetic modeling, which requires a blood input function. For dynamic imaging of brain or head and neck cancer on a conventional 20-30 cm-long PET scanner, an input function is generally obtained through arterial blood sampling, which is invasive and requires considerable effort. Alternatively, image-derived input function (ID-IF) from intracranial blood vessels such as carotid arteries suffer from severe partial volume effect. We developed a kernel-based simultaneous estimation (SIME) method that allows joint estimation of optimization-derived input function (OD-IF) and kinetic parameters. While evaluating this method is challenging on conventional short PET scanners, here we used the uEXPLORER total-body PET system that covers major blood pools to provide a reference for validation with human subjects dataset.

Methods:

Standard SIME method estimates an input function and kinetic parameters simultaneously by fitting multiple tissue time activity curves (TACs) of different regions of interest. Our proposed kernel SIME method further exploits ID-IF as a *priori* information using a kernel representation. For evaluation, datasets consist of 7 subjects scanned on the uEXPLORER total-body PET/CT system with 18F-FDG were used to compare estimated input function from our kernel SIME method with ID-IF. The data were acquired for 60 minutes with 29 time frames. TACs from gray matter (GM), white matter (WM), and cerebrospinal fluid (CSF) as measurements for the kernel SIME. The TAC from the carotid artery was used as the ID-IF and the TAC from the descending aorta as the reference IF. For both ID-IF and OD-IF methods, the last time point was scaled to the reference IF to overcome the scaling problem. Different IFs were compared for quantification of FDG delivery rate K_1 , fractional blood volume f_v , and net influx rate K_i .

Results:

The estimated OD-IF by kernel SIME show a good match with the reference input functions in all subjects. Compared to ID-IF, estimated kinetic parameters with OD-IF have higher correlations (OD-IF: 0.82 for K_1 , 0.77 for f_v , 0.93 for K_i ; ID-IF: 0.73 for K_1 , 0.54 for f_v , 0.93 for K_i) and lower percentage mean absolute error (MAE) (OD-IF: 36.8% for K_1 , 26.8% for f_v , 17.6% for K_i ; ID-IF: 127.5% for K_1 , 119.0% for f_v , 47.0% for K_i). Parametric images with OD-IF show similar patterns and close values as those with the reference IF.

Conclusion:

We proposed and investigated a kernel SIME method to obtain OD-IF. Studies using total-body patient datasets indicate the method enables more accurate estimation of input function and kinetic parameters for brain PET imaging as compared to ID-IF.

Qualitative and Quantitative Validation of a Scatter Correction Method for Total-Body Positron Emission Tomography

Presenter: R. Bayerlein¹ (post-doctoral researcher), Advisor: R. D. Badawi^{1,2}

Co-authors: Z. Xie², E. K. Leung^{1,2,3}, Y. G. Abdelhafez¹, B. A. Spencer^{1,2}, N. Omidvar², Q. Wang², E. Li², L. Nardo¹, S. R. Cherry^{2,1}

¹Department of Radiology, UC Davis Health, Sacramento, CA, USA

²Department of Biomedical Engineering, University of California Davis, CA, USA

³UIH America, Inc., Houston, TX, USA

I. INTRODUCTION

Total-body positron emission tomography (PET) is a powerful molecular imaging tool with the ability to scan the entire body in one bed position, and enables novel applications in the clinic and research. The uEXPLORER is a total-body PET scanner with an axial field of view (FOV) of 194 cm, which provides improved image quality for static and dynamic PET imaging [1], a spatial resolution of about 3.0 mm, and a 15-68-fold increase in sensitivity [2] compared to conventional PET scanners with shorter axial FOV. However, the large number of detectors and the widened acceptance angles dramatically increase dataset sizes, setting higher demands on image reconstruction algorithms and data correction techniques. Specifically, the correction of scattered events, which degrade contrast and quantitative accuracy in reconstructed PET images [3] becomes more complex and computationally expensive. In this contribution we will present the recently developed Monte Carlo-based scatter correction method embedded in our in-house PET image reconstruction framework, and will provide a qualitative and quantitative image quality assessment using phantom and human subject data.

II. METHODS

A. The Scatter Correction Method

The SC method was first developed using the simulation toolkit SimSET [4]. Images were reconstructed using the 3D-TOF-OSEM algorithm with point spread function modeling, 2.85 mm isotropic voxel size, corrections for attenuation, dead-time, and random events, and without image post-processing filters. Scatter estimation was performed after every OSEM iteration using 10^{10} events simulated with SimSET using 48 CPU threads in parallel. The SC factors for every list-mode event were calculated and incorporated into the next image estimate. Simulated sinograms were scaled to measured sinograms, which were normalized and corrected for random events and dead time prior to scaling. Each event was binned into 273 ps sized TOF bins and scaling was done for each TOF bin individually.

B. Means of Validating the Framework

Besides visual confirmation of the correction of scatter in the reconstructed images, the image quality was quantitatively assessed using a phantom scan following the NEMA NU 2-2018 protocol.

For further validation, an 83 y/o patient with lung cancer was scanned for 20 mins at 120 mins after intravenous injection of 373.7 MBq of [¹⁸F]FDG, and reconstructed with the above parameters. Affirmation of SC was performed with various methods. The general diagnostic image quality was assessed by investigating lesion conspicuity, especially in metastases in adrenal glands and lymph nodes of the lung cancer patient. The average peak-to-valley-ratio (PVR) along a line profile through

the center of 13 vertebrae was calculated. Scatter removal in the trachea was quantified using the average activity concentration in comparison to lung tissue.

III. RESULTS

The contrast recovery coefficient (CRC) in the phantom scans ranged from 57.9% for the smallest sphere (10 mm diameter) to 89.9% for the largest sphere (37 mm). Without scatter correction the CRC was 50.3% for the smallest and 71.7% for the largest sphere. A residual error in the lung insert of 5.9% and 17.0% was found with and without SC, respectively.

Fig. 1 shows Maximum Intensity Projections (MIPs) of the total-body PET scan of a patient with metastatic lung cancer without SC (#1) and with SC (#2). In the uncorrected image the contribution of scatter is very noticeable in the abdominal region and impairs lesion conspicuity, whereas the contrast in the scatter corrected image is apparently higher. The PVR in the spine in the scatter corrected image was 3.46 compared to 1.98, without SC. Despite a small residual scatter contamination inside the trachea the average activity concentration was 31.0% lower than in lung tissue (6.9% lower without SC).

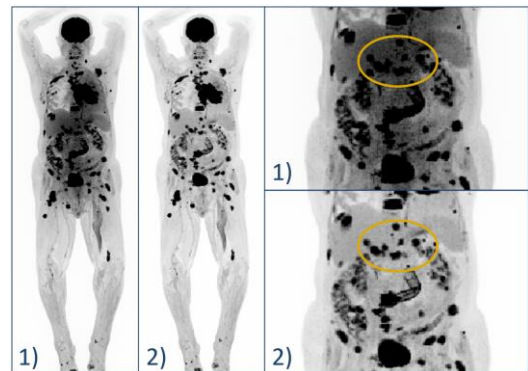


Fig. 1. MIPs of a total-body PET scan of a human subject without SC (#1) and with SC (#2). The orange oval contours the region with the most noticeable changes.

IV. DISCUSSION AND CONCLUSION

A SC technique was successfully implemented in our in-house reconstruction framework and quantitatively and qualitatively validated. Images of human subjects showed largely increased lesion conspicuity and improved quality compared to uncorrected images. These results could serve as a ground truth for optimizing the performance and efficiency of future SC methods.

REFERENCES

- [1] Badawi et al., 10.2967/jnumed.119.226498
- [2] Spencer et al., 10.2967/jnumed.120.250597
- [3] Zaidi et al., 10.1016/j.cpet.2007.10.003
- [4] E. Leung et al., JNM, 2021, 62 (supplement 1)

A Cross-Attention Method Based on Tumor-Feature-Templates for Segmenting Small Liver Tumors in CT Scans

Purpose/Objective(s)

Liver cancer is one of the leading causes of cancer death. Accurate detection of liver cancer early using CT could assist doctors in disease diagnosis and treatment planning. This study proposes a deep learning method for accurate detection and segmentation for liver tumors, especially for **small** liver tumors.

Materials/Methods

This study included 131 CTs of patients with liver cancer. We hypothesize that liver tumors of different sizes share similar imaging characteristics in the feature space. The information of known tumors can compensate for the information loss of small tumors from the feature propagation, which can improve small tumor segmentation. Our method first constructs a liver tumor template by all CT slices containing tumors in the training set, then extracts the semantic features of input CT image and tumor template simultaneously by using two residual networks. Finally, the relationship between input CT and tumor template in the feature space is exploited to improve liver cancer segmentation.

Results

Among 20,693 CT slices of the 31 testing patients, all CT slices were separated into groups according to tumor size as follows: 0.1–2.0 (3.17%), 2.1–5.0 (3.58%), 5.1–10.0 (3.13%), and 10.1–20.0 (3.01%) cm. Other slices without tumor or tumor size > 20 cm were categorized as another same group. Our method outperforms state-of-the-art models including Unet, PAN, DeepLabV3, FPN, LinkNet, and PSPNet on different sizes of tumors, especially for small liver tumor segmentation. For the 10.1-20cm liver tumor, our method achieved 7.1%, 1.9%, 2.9%, 3.8%, 3.3%, 1.3% improvement, and on the 0.1-2.0cm small liver tumor set, our method achieved 8.4%, 10.0%, 11.3%, 9.1%, 10.9%, and 9.6% improvement, respectively.

Conclusions

This work indicates tumors of different sizes share similar imaging characteristics. The small-large tumors relation can significantly improve small liver tumor segmentation, which is beneficial for disease diagnosis and treatment planning.

Supporting document for

A Cross-Attention Method Based on Tumor-Feature-Templates for Segmenting Small Liver Tumors in CT Scans

Innovation/Impact: We consider this study to be innovative because it's the first work exploiting the relation between small tumors and existing different sizes of tumors in the feature space to improve the small liver tumor segmentation. The small-large tumors relation can significantly improve small liver tumor segmentation, which is beneficial for disease diagnosis and treatment planning and has the potential for other types of tumor detection and segmentation.

Key Results: Figure 1 is the framework of our method, as shown in the figure, our method exploits the relation between input CT image and the constructed liver tumor template to improve liver segmentation. The test experiments are conducted in 131 patients with liver cancers. Table 1 shows the distribution of tumor size, from the table we could know small tumors (0.1-5.0 cm) account for about 10 percent of the total number of tumors. Table 2 shows the results of our method and comparing methods on different sizes of tumors. As show in table 2, our method outperforms all other methods on liver tumor segmentation, especially for small liver tumors.

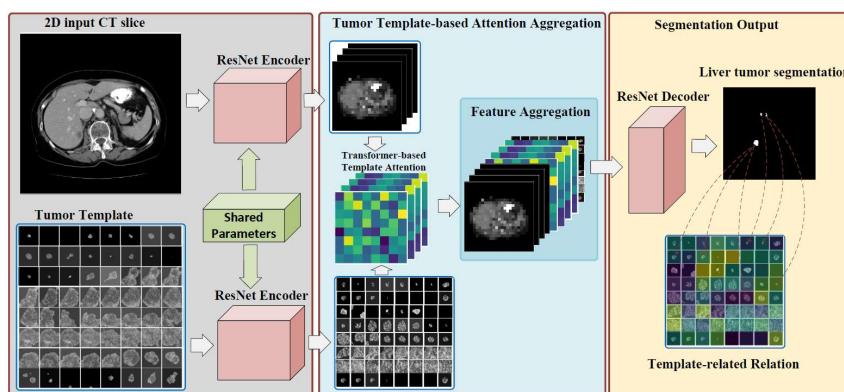


Figure 1. The framework of the Tumor Feature Template-based Cross-Attention Method.

Table 1. The number of tumor sizes in the dataset.

Tumor size (cm)	0.1-2.0 N (%)	2.1-5.0 N (%)	5.1-10.0 N (%)	10.1-20.0 N (%)	0 or ≥20.1 N (%)
Train	1545 (3.77%)	1485 (3.62%)	1261 (3.08%)	630 (1.54%)	36068 (87.99%)
Val	146 (2.89%)	278 (5.50%)	87 (1.72%)	95 (1.88%)	4445 (88.00%)
Test	399 (3.17%)	451 (3.58%)	394 (3.13%)	379 (3.01%)	10963 (87.10%)
All	2090 (3.56%)	2214 (3.78%)	1742 (2.97%)	1104 (1.88%)	51476 (87.80%)

Table 2. The segmentation performance (Dice score per case) on different sizes liver tumors.

Tumor size (cm)	0.1-2.0	2.1-5.0	5.1-10.0	10.1-20.0	0 or ≥20.1	ALL
Unet	0.417	0.516	0.549	0.581	0.671	0.651
PAN	0.401	0.483	0.579	0.633	0.694	0.672
DeepLabV3	0.388	0.517	0.560	0.623	0.661	0.643
FPN	0.410	0.455	0.552	0.614	0.709	0.683
LinkNet	0.392	0.478	0.554	0.619	0.688	0.665
PSPNet	0.405	0.505	0.556	0.639	0.677	0.657
Ours	0.513	0.571	0.609	0.652	0.711	0.695

SLAM competitions

Neeladrisingha (Neel) Das (Stanford)

- **Cell GPS: Tracking cancer metastasis in real-time**

Tushar Shinde (Stanford)

- **Neighbors, Trip and Packing**

Shengtian Sang (Stanford)

- **Using deep connections to make model see more clearly**

Jose Ramos-Mendez (UC Francisco)

- **Chasing FLASH (the mechanism)**

Meghan Keohane (UC Davis)

- **Which ultrasound imaging mode can localize the needle better**





AND THE AWARD GOES TO